Supplementary Information: Enhancing Cation Diffusion and Suppressing Anion Diffusion via Lewis-Acidic Polymer Electrolytes

Brett M. Savoie, Michael A. Webb, Thomas F. Miller III

Division of Chemistry and Chemical Engineering, California Institute of Technology

Pasadena, California 91125, United States

January 8, 2017

Contents

1 Computational Methods

1.1 Molecular Dynamics

The molecular dynamics (MD) simulations employed a non-polarizable force-field that was systematically parameterized using the Topologically Automated Force-Field Interactions (TAFFI) methodology; a summary of the methodology is provided here with additional comprehensive details provided in the later sections.

All intramolecular modes, atomic partial charges, and ion-polymer Lennard-Jones parameters were parameterized in this work to provide a consistent description of all polymers. Intramolecular modes, such as bonds, angles, and dihedrals, were parameterized by fitting standard harmonic and fourier potential energy terms to mode-scans performed at the B3LYP-D3/def2-TZVP level. For each polymer, a model compound comprised of a tetramer of the polymer capped with methyl groups was employed for the intramolecular mode parametrization. Approximate atomic partial charges were obtained from CHELPG calculations based on the B3LYP-D3/def2-TZVP electron densities at the optimized geometries. After obtaining the intramolecular modes and approximate partial charges, condensed phase MD simulations were performed on the pure oligomers and also solutions with each salt to provide configurations to further refine the atomic partial charges and parametrize the dispersion interactions. Final partial charges on each atom were determined by averaging the results of CHELPG calculations based on the B3LYP-D3/def2-TZVP electron densities for one hundred molecular configurations sampled from condensed phase MD trajectories. Pairwise molecular configurations sampled from the condensed phase MD trajectories were used to parametrize the dispersion contributions to the polymer-polymer, ion-polymer, and ion-ion interactions. The dispersion interactions were parameterized by fitting Lennard-Jones potentials to the residual of the fixed electrostatic interactions and the counter-poise corrected B3LYP-D3/def2-TZVP interaction energies calculated for the pairwise configurations. Full parametrization details, parameter tables, mode scans, and fit potentials are included in later sections.

All MD simulations were performed within the LAMMPS software suite.[1] All trajectories employed periodic boundary conditions, particle-particle-particle-mesh (pppm) evaluations of long-range interactions beyond a 14 Å cut-off, a Nosé-Hoover barostat with 1000 fs relaxation, and a Nosé-Hoover thermostat with 100 fs relaxation (NPT). Equations of motion were evolved using the

velocity-Verlet integrator and a two femtosecond timestep for polymers without explicit hydrogen atoms and a one femtosecond timestep for polymers with explicit hydrogen atoms. Intramolecular pairwise interactions for atom pairs connected by fewer than four bonds were excluded during the MD simulations to avoid double counting with dihedral energy terms. Ion diffusion and solvation free energy trajectories were initialized from a common set of four independently equilibrated neat polymer trajectories. Each neat polymer trajectory included a single polymer chain with a mass of approximately 30 kDa that was initialized using a protocol to randomize chain orientation and avoid configurations with significant overlap between atoms. These configurations were initially equilibrated at a temperature of 10 K and a pressure of 50 atm for 50 ps, followed by a 10 ns annealing phase at a temperature of 500 K and a pressure of 1 atm. After annealing, the configurations were simulated for 11 ns at a temperature of 400 K and a pressure of 1 atm to collect production data. The first nanosecond of the production trajectories was used for equilibration and the remaining 10 ns were used to confirm the convergence of the density. The final configurations from the neat polymer trajectories were used as input geometries for the ion diffusion and solvation free energy trajectories.

1.2 Ion Diffusion Simulations

For each combination of ion and polymer, sixteen independent ion-diffusion trajectories were performed. These trajectories were initialized from the four pre-equilibrated neat polymer trajectories by randomly inserting a single ion into each configuration (four independent insertions for each pre-equilibrated configuration). Each trajectory included a single ion to avoid correlated ion motions, and the excess charge was neutralized with a uniformly distributed background charge. The initial geometry was relaxed by performing 1 ps of NVE dynamics with atom displacements limited to 0.01 Å for each timestep, followed by 1 ns of NPT dynamics at a temperature of 400 K and pressure of 1 atm. After relaxation, an additional 300 ns of NPT dynamics were performed to collect production data. A total of 4.8 μs of ion diffusion dynamics were collected for each ion in each polymer (16 independent trajectories, each 300 ns long).

Diffusivities can be calculated from the long-timescale trajectories using the Einstein equation

$$D_i = \lim_{t\to\infty} \frac{\mathrm{d}\left\langle |\mathbf{r}_i(t) - \mathbf{r}_i(0)|^2 \right\rangle}{6\mathrm{d}t}, \tag{1}$$

where D_i is the diffusion coefficient for ion, i, and the term in brackets is the MSD evaluated at time t. Because many of the systems studied still exhibit sub-diffusive behavior even at long times, apparent diffusivities are reported by approximating the derivative in Eq. (1) by finite difference using the MSD at $t = 150$ and $t = 0$ ns.[2,3] The Li^+ transference number, T_{Li}, was calculated using $T_{\mathrm{Li}} = D_{\mathrm{Li}}/(D_{\mathrm{Li}} + D_{\mathrm{anion}})$.

Contact durations were calculated by defining a characteristic function, $h_{ij}(t)$, that reports on contacts between pairs of atoms

$$h_{ij}(r) = \begin{cases} 1 & ,\text{for } r_{ij} \leq r_{\mathrm{T}} \\ 0 & ,\text{for } r_{ij} > r_{\mathrm{T}} \end{cases}, \tag{2}$$

where i and j denote atomic indices, and r_{T} is a pair-specific threshold distance, which is chosen based on the size of the first coordination shell for the corresponding atom types. Specifically, $r_{\mathrm{T}} = r_{\max} + 2\sigma$, where $r_{\max}$ is the radial separation at the first maximum of the corresponding ion-polymer radial-distribution function (see Supporting Information), and σ is the standard deviation obtained by fitting the full width at half maximum of the peak to a Gaussian function. The

time autocorrelation function, $\langle h_{ij}(0)h_{ij}(t)\rangle$, was calculated for each contact type by averaging the trajectories with respect to time. Standard errors were calculated by separately averaging the results from the sixteen independent trajectories.

1.3 Solvation Free-Energy Calculations

Thermodynamic integration was used to calculate the ion-specific solvation free energies in each polymer.[4] For each combination of ion and polymer, sixteen independent ion-insertion trajectories were used. Scaled potentials were used to gradually introduce the ion-polymer potential energy terms, and convergence was facilitated by introducing the polymer-ion Lennard-Jones interactions before introducing the polymer-ion electrostatic interactions. A scaled potential was used to first introduce the polymer-ion Lennard-Jones interactions

$$U_{\mathrm{LJ}}(\lambda_1) = U_{\mathrm{P}} + \lambda_1 \left(U_{\mathrm{P+X_{LJ}}} - U_{\mathrm{P}}\right) , \tag{3}$$

where λ_1 is the scaling parameter, U_{P} is the potential of the pure polymer, and $U_{\mathrm{P+X_{LJ}}}$ is the potential of the pure polymer plus ion-polymer Lennard-Jones interactions. Standard λ-dependent soft-core Lennard-Jones potentials, as implemented in LAMMPS with $n = 1$ and $\alpha_{\mathrm{LJ}} = 0.5$, were used for all ion-polymer interactions to smooth the potential energy function.[5] When $\lambda_1 = 0$, the ion and polymer are non-interacting, and when $\lambda_1 = 1$, the ion-polymer Lennard-Jones terms fully contribute to the potential energy. A second scaled potential was used to subsequently introduce the polymer-ion electrostatic interactions

$$U_{\mathrm{C}}(\lambda_2) = U_{\mathrm{P+X_{LJ}}} + \lambda_2 \left(U_{\mathrm{P+X_{LJ}+X_C}} - U_{\mathrm{P+X_{LJ}}}\right) , \tag{4}$$

where $U_{\mathrm{P+X_{LJ}+X_C}}$ is the potential of the polymer plus all polymer-ion interactions. The potential in Eq. (4) was implemented by using λ-scaled charges on the ion. When $\lambda_2 = 0$, the ion and polymer interact only through the Lennard-Jones potential, and when $\lambda_2 = 1$, both the ion-polymer electrostatic and Lennard-Jones terms fully contribute to the potential energy. The total solvation free-energy was obtained by

$$\Delta G_{\mathrm{TI}} = \int_0^1 \left\langle \frac{\mathrm{d}U_{\mathrm{LJ}}}{\mathrm{d}\lambda_1} \right\rangle \mathrm{d}\lambda_1 + \int_0^1 \left\langle \frac{\mathrm{d}U_{\mathrm{C}}}{\mathrm{d}\lambda_2} \right\rangle \mathrm{d}\lambda_2 \, . \tag{5}$$

The brackets in Eq. (5) indicate an ensemble average, and the approximation has been made that the $P\Delta V$ contribution to the free energy change can be safely neglected. The integrals in Eq. (5) were evaluated numerically using the trapezoidal rule, with λ_1 and λ_2 incremented in steps of 0.1 (twenty-one steps total, eleven for the Lennard-Jones phase and eleven for the electrostatics, less one redundant step connecting the two phases). The system was allowed to equilibrate for 100 ps at each λ-step, then an additional 100 ps of dynamics were used for calculating the necessary derivatives. The derivatives in Eq. (5) were calculated by finite-difference. At endpoints, forward or backward finite-difference was used, at all other points the central difference was used with a λ-step of 0.01 to evaluate the derivative. In the case of TFSI^-, an additional free energy contribution associated with removing the intramolecular electrostatics must be computed. Free-energy perturbation was used to evaluate this contribution from a ten ns MD trajectory of a single TFSI^- molecule in vacuum. The reported ΔG_{TI} values were calculated as the average over all ion-insertion trajectories, with errors in the mean estimated by bootstrap resampling (5 million samples).[6]

It is common for borane centers to undergo changes in bonding hybridization and associated structural rearrangements upon anion complexation.[7] Since these effects are not captured by the force-field used in this work, it is anticipated that the MD thermodynamic integration calculations

significantly underestimate the anion solvation free energies in the Lewis-acidic polymers. Using *ab initio* geometry optimizations and energy calculations, we thus include a free-energy-perturbation correction to the solvation free energy (for both the Lewis-acidic polymers and PEO) associated with local structural relaxation during anion complexation,

$$\Delta G_{\mathrm{corr}} = \Delta G_{\mathrm{rel,anion}} - \Delta G_{\mathrm{rel,neat}}, \tag{6}$$

where

$$\Delta G_{\mathrm{rel,anion}} = -\beta^{-1} \ln \left\langle e^{-\beta \Delta U_{\mathrm{rel,anion}}} \right\rangle \tag{7}$$

accounts for the free-energy change in the anion-polymer system upon relaxation, and

$$\Delta G_{\mathrm{rel,neat}} = -\beta^{-1} \ln \left\langle e^{-\beta \Delta U_{\mathrm{rel,neat}}} \right\rangle \tag{8}$$

accounts for the corresponding effect in the neat polymer. The angle brackets in Eqs. (7) and (8) correspond to ensemble averaging over the MD configurations, and the configuration-specific relaxation energies $\Delta U_{\mathrm{rel,anion}}$ and $\Delta U_{\mathrm{rel,neat}}$ are obtained from quantum chemistry calculations at the PBE-D3/def2-SVP level of theory, as described below.

The $\Delta U_{\mathrm{rel,anion}}$ terms in Eq. (7) were calculated by performing constrained geometry optimizations of the anion solvation structures. For each anion in each polymer, ten solvation snapshots were extracted at 100-picosecond intervals from the dilute ion concentration MD trajectories. Each solvation snapshot consisted of the anion and all polymer atoms within $r_{\mathrm{outer}} = 5\,\text{Å}$ of any anion atom. The value of r_{outer} was chosen to be large enough to include the first solvation shell for all combinations of polymer and anion ($r_{\mathrm{inner}} = 4.5\,\text{Å}$, see Fig. S1) plus a buffer region of 0.5 Å. The united-atom moieties and the terminal atoms of polymer fragments in the solvation snapshot were then hydrogenated, and a constrained geometry optimization of the added hydrogens was performed. Subsequently, a constrained geometry optimization was performed in which all binding atoms (carbon for PEO and boron for all Lewis-acidic polymers) within r_{inner} of any anion atom and polymer atoms within two bonds of those binding atoms were relaxed, while the positions of all anion atoms and remaining polymer atoms were constrained. For instances where these cutoff values return a polymer fragment without any constrained atoms, a position constraint was placed on the atom in the fragment farthest from the anion. The relaxation energy, $\Delta U_{\mathrm{rel,anion}}$, is obtained from the single-point energy difference for the system before and after the constrained geometry optimization. For each combination of polymer and anion, the average number of polymer binding atoms that were within r_{inner}, N_{poly}, is determined, and this value is used in the protocol for the calculation of $\Delta U_{\mathrm{rel,neat}}$.

The $\Delta U_{\mathrm{rel,neat}}$ terms in Eq. (8) were similarly calculated by performing constrained geometry optimizations of snapshots obtained from neat-polymer MD trajectories. The procedures for sampling and optimizing the neat polymer snapshots were identical to the solvation geometries, except that the neat polymer snapshots included all polymer atoms within $r_{\mathrm{outer}} = 7.5\,\text{Å}$ of the center of the simulation box; this larger value of r_{outer} was used in the neat-polymer calculations to account for the reduced density of binding atoms in the neat-polymer snapshots relative to the anion-containing snapshots. During the geometry relaxation, only the N_{poly} binding atoms closest to the center of the simulation box and the polymer atoms within two bonds of those binding atoms were allowed to relax, where N_{poly} is defined above; this ensures that the same average number of binding atoms are relaxing in calculating both $\Delta U_{\mathrm{rel,anion}}$ and $\Delta U_{\mathrm{rel,neat}}$. The neat relaxation energy, $\Delta U_{\mathrm{rel,neat}}$, is obtained from the single-point energy difference for the system before and after the constrained geometry optimization.

The final expression used to evaluate the solvation free energy for an anion was

$$\Delta G_{\mathrm{S}} = \Delta G_{\mathrm{TI}} + \Delta G_{\mathrm{corr}}. \tag{9}$$

Table S1 includes the values of ΔG_{corr} for all anions in all polymers. For Li^+ in all polymers, $\Delta G_{\mathrm{S}} = \Delta G_{\mathrm{TI}}$.

1.4 Salt Lattice Energies

The salt lattice energies for LiCl and LiTriflate presented in Fig. 5b were taken from reference 16. No experimental reference exists for LiTFSI, so the lattice energy was estimated using a modified Kapustinki approach[8] developed by Jenkins and a volume of 136.1 $Å^3$ for TFSI calculated based on the DFT optimized structure at the B3LYP-D3/def2-TZVP level.

2 Results Referenced in the Main Text

2.1 Dilute Simulations for All Ions and Polymers

Fig. S1 shows the ion-polymer radial distribution functions $g_{AB}(r)$ for all ions in all polymers simulated in the dilute-ion regime. For each ion-polymer combination, $g_{AB}(r)$ is calculated such that A refers to the set of atoms associated with the ion and B refers to the set of atoms associated with the polymer that have partial charges with opposite sign as the ion.

Fig. S2 shows the mean-squared displacement (MSD) for all ions, primary ion-polymer contact durations, and the MSDs of the polymer segments calculated from the dilute-ion simulations at 400 K. The data for Li^+ and Cl^- are reproduced from the main text for comparison.

2.2 Finite Salt Concentration Simulations

All finite salt concentration simulations were initialized using the same equilibrated neat polymer configurations that were used to initialize the dilute-ion simulations, as described in the main text. Ions were added to the neat polymer configurations at random positions until reaching the specified concentration. The initial geometry was relaxed by performing 5,000 energy minimization steps, during which the displacements of each atom were limited to 0.01 Å per step, followed by 5 ns of NPT dynamics at a temperature of 400 K and pressure of 1 atm. After relaxation, NPT dynamics at a temperature of 400K and pressure of 1 atm were run for an additional 75 ns (using a 1 fs timestep) for polymers with explicit hydrogen atoms and 150 ns (using a 2 fs timestep) for all other polymers. A Nosé-Hoover thermostat (100 fs relaxation timescale) and barostat (1000 fs relaxation timescale) were used to control the temperature and pressure for all NPT simulations. Sixteen independent trajectories were simulated per electrolyte at each concentration.

The ion force-fields were parametrized in the dilute limit and are not expected to be quantitatively valid at finite salt concentrations, where polarizability plays an important role. Simulations of polymer electrolytes at high salt concentrations have also been shown to exhibit increased aggregation and suppressed conductivity relative to experiment when using non-polarizable or fixed-charge force fields.[9–13] Likewise, initial simulations with full charges on the ions showed negligible conductivity and failed to reach equilibrium even at long (75 ns) timescales (not shown). To obtain reduced pairing and mobile ion dynamics, the charges on the ions were uniformly scaled by 0.5 during the simulation, similarly to previous work.[9–12] Any attempt to compare the ion-pairing results in Fig. S3 with the dilute ion concentration solvation free energies in Fig. 5 of the main

text should consider that the finite-concentration results in Fig. S3 are simulated with scaled point charges and do not include intramolecular relaxation corrections like those used in Fig. 5.

Fig. S3 shows the conductivity (σ), degree of uncorrelated ion motion (α), and transference number (T_{Li}) for each polymer with LiTFSI at two concentrations (r=0.1 and r=0.05, where r is the ratio of Li^+ ions to polymer monomer units) and scaled partial charges on the salt. The conductivity was calculated according to

$$\sigma = \lim_{t\to\infty} \frac{e^2}{6tVk_{\mathrm{B}}T} \sum_{ij}^{N} z_i z_j \left\langle \mathbf{d}_i(t)\mathbf{d}_j(t) \right\rangle, \tag{10}$$

where e is the fundamental charge, V is the simulation volume, T is the temperature, z is the integer charge of the ion, $\mathbf{d}$ is the vectorial displacement of the ion at time t, the i and j indices run over all ions in the simulation, and N is the total number of ions in the simulation box. When calculating σ, the charges on all ions were unscaled.

The degree of uncorrelated ion motion, α, was calculated according to

$$\alpha = \lim_{t\to\infty} \frac{1}{6t\left(D_{\mathrm{Li}} + D_{\mathrm{anion}}\right)N} \sum_{ij}^{N} z_i z_j \left\langle \mathbf{d}_i(t)\mathbf{d}_j(t) \right\rangle, \tag{11}$$

where D_{Li} and D_{anion} correspond to average the diffusivity of Li^+ and the anion, respectively, calculated as

$$D_\beta = \lim_{t\to\infty} \frac{1}{6t} \sum_{i\in\beta} \left\langle \mathbf{d}_i(t)\mathbf{d}_i(t) \right\rangle, \tag{12}$$

and the summation in Eq. 3 runs over all ions of type β. When the cross terms in the summation in Eq. 2 average to zero (i.e., uncorrelated ion motion), then α equals one. When Li^+ motion perfectly correlates with anion motion (i.e. paired behavior), α equals zero. As in the main text, T_{Li} was calculated according to

$$T_{\mathrm{Li}} = \frac{D_{\mathrm{Li}}}{D_{\mathrm{Li}} + D_{\mathrm{anion}}}. \tag{13}$$

The limit on t was taken as 75 ns when calculating all quantities. The data shown in Fig. S3 represents averages over all trajectories (16 trajectories per electrolyte), with the error bars representing the standard error for each quantity calculated across all trajectories.

Table S1: Free energy corrections, ΔG_{corr}, associated with structural relaxations during anion complexation for all anions in all polymers.

	Cl^-	Triflate	TFSI
PEO	-10 ± 4	-14 ± 9	-1 ± 6
CBC	-37 ± 6	-19 ± 6	-74 ± 14
CBCC	-100 ± 9	-28 ± 8	-26 ± 5
HBC	-83 ± 14	-10 ± 10	-33 ± 14
HBCC	-67 ± 13	-41 ± 15	-61 ± 8

Units in $\mathrm{kcal \cdot mol^{-1}}$.

Standard errors are reported.

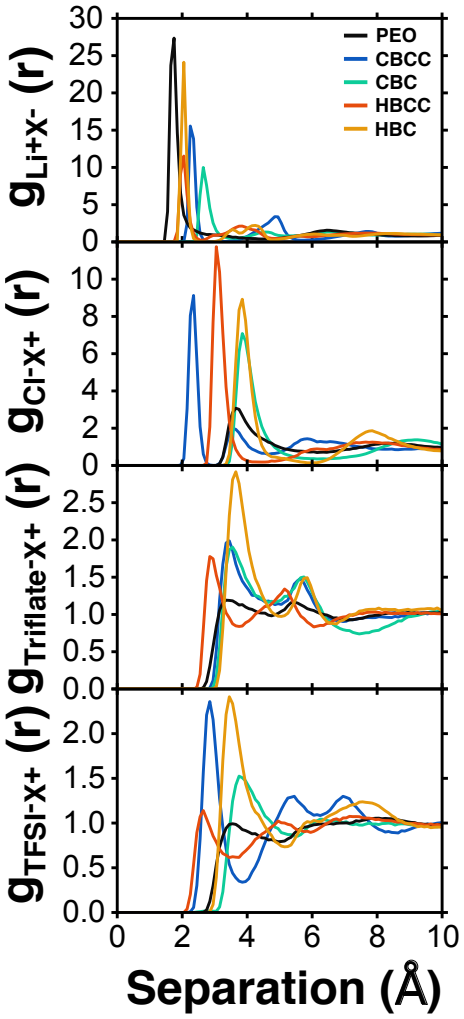

Figure S1: Comparison of radial-distribution functions (RDFs) for all ions in all polymers simulated in the dilute-ion regime at 400 K. "X" in each case includes all polymer atoms of opposite partial charge as the ion. The data are represented as a histogram with a bin width of 0.1 Å for r.

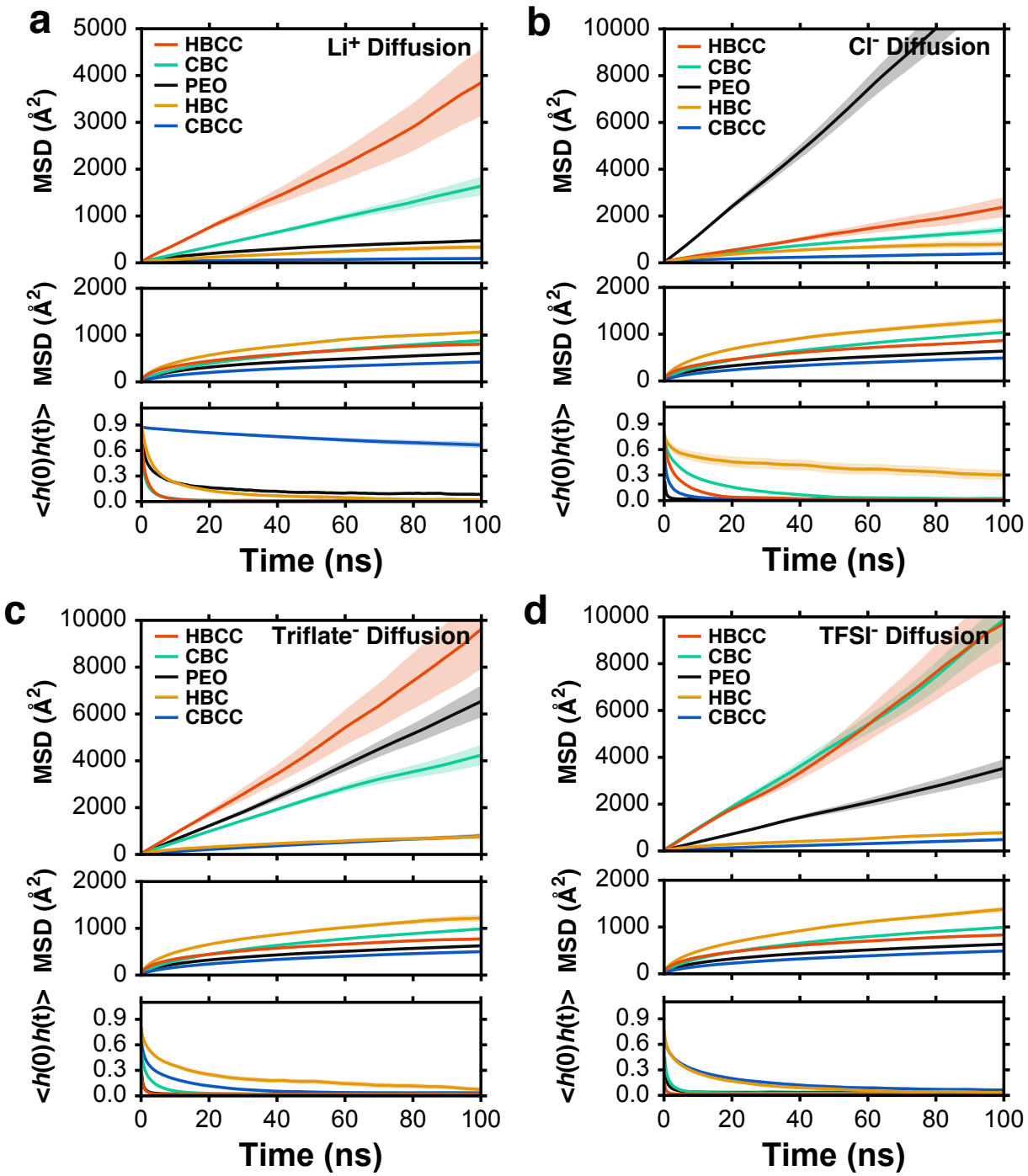

Figure S2: Contrasting ion transport behavior in Lewis-basic and Lewis-acidic electrolytes. In each panel, the top plot shows the mean squared displacement (MSD) of the ion in each polymer, the middle plot shows contact durations for the ion and its predominant binding atom in each polymer (for Li^+ this corresponds to O in PEO, CH_3 in CBC, CH_2 in CBCC; and H in HBC and HBCC; for all anions this corresponds to CH_2 in PEO and B in all Lewis-acid polymers), and the bottom plot shows the MSD of the polymer monomer units in each simulation. All data is derived from MD trajectories at 400 K in the dilute-ion regime. Average values are plotted as solid lines and standard errors are plotted as shaded regions.

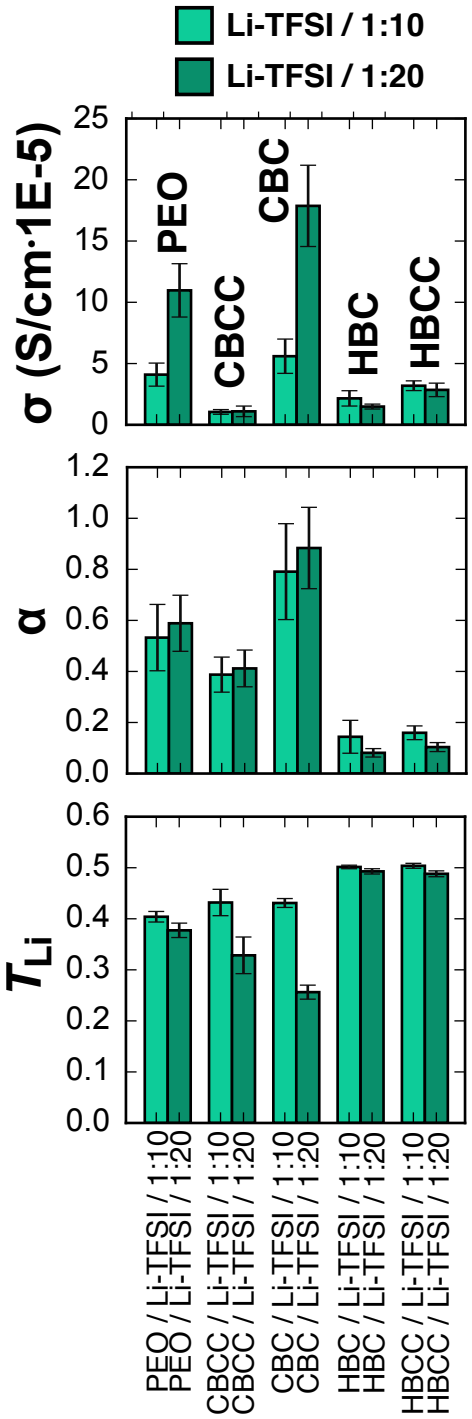

Figure S3: Results from finite salt concentration simulations at 400 K. (top) Net conductivity (σ), (middle) degree of uncorrelated ion motion (α), and (bottom) Li^+ transference number (T_{Li}) for Li:TFSI with each polymer in this study. The concentrations refer to the ratio of Li^+ to polymer monomer units.

3 Parametrization Details

3.1 Force-Field Details

The non-polarizable TAFFI force-field used in all simulations employed the optimized potentials for liquid simulations (OPLS) functional forms for the stretching, bending, pair-wise, and torsional potentials. The total force field energy, E_{FF}, is expressed as,

$$E_{\mathrm{FF}} = \sum_{\text{bonds}} k_{\mathrm{r}} \left(r - r_0\right)^2 + \sum_{\text{angles}} k_\theta \left(\theta - \theta_0\right)^2 + \sum_{\text{dihedrals}} \sum_{i=1}^{4} \frac{1}{2} V_i \left(1 + (-1)^{i+1} \cos(i\phi)\right) + \sum_{i>j} \left\{ \frac{q_i q_j e^2}{4\pi\epsilon_0 r_{ij}} + 4\epsilon_{ij} \left[\left(\frac{\sigma_{ij}}{r_{ij}}\right)^{12} - \left(\frac{\sigma_{ij}}{r_{ij}}\right)^{6} \right] \right\}, \quad (14)$$

where k_{r} and r_0 are the bond-specific force constant and equilibrium displacement, respectively; k_θ and θ_0 are the angle-specific force constant and equilibrium angle, respectively; the V_i terms are dihedral-specific Fourier coefficients, r_{ij} are the interatomic separations, q_i are the partial atomic charges, e is the elementary charge, and ϵ_{ij} and σ_{ij} are the Lennard-Jones parameters for each pairwise interaction. The summation for the Lennard-Jones and Coulomb potentials runs over all intermolecular atomic pairs and all intramolecular atomic pairs separated by more than three bonds. Carbon and its attached hydrogens (UA-H) were modeled as united atoms; hydrogens bonded with boron were modeled as explicit atoms. For charge parametrization, the charge of each carbon was calculated by including the nuclear charges of any attached hydrogens.

3.2 Fitting Procedure for Intramolecular Modes

All quantum chemistry calculations were performed at the B3LYP-D3/def2-TZVP level of the theory,[14,15] unless otherwise noted. For calculations involving anions, the minimally augmented diffuse basis set ma-def2-TZVP was used.[16] For each polymer, a model compound comprised of a tetrameric unit of the polymer capped by methyl groups was employed for parametrization. The model compounds were initialized in an all-*trans* geometry and geometry optimized followed by a frequency calculation to confirm minimization; a similar procedure was used for polyatomic anions without constraints on the initial dihedral angles. At each optimized geometry, the calculated electron densities were used for CHELPG calculations[17] to obtain nuclear charges, with averaging performed over like atom types. The CHELPG charges obtained from the optimized geometry were used as an initial guess for initially parametrizing the dihedral potentials and performing the condensed phase MD simulations (see below). The optimized geometries were then used to perform constrained mode scans of each unique bond, stretch, and dihedral. Bond mode scans consisted of compression and extension ± 0.1 Å about the optimized bond length in steps of 0.02 Å; angle mode scans consisted of compression and expansion by 5° about the optimized angle in steps of 1°; dihedral mode scans consisted of rotation by ±180° about the optimized angle in steps of 10°. For dihedral scans, a fragment was built from the optimized model compound by substituting non-terminal atoms separated by more than two bonds from the 2-3-atoms of the dihedral with hydrogen atoms and removing all further separated atoms. Geometry optimizations of each scan configuration were performed with the mode being parameterized constrained to a fixed value while optimizing all remaining degrees of freedom. Force constants for each stretch and bend were obtained by performing numerical least-squares fitting (Levenberg-Marquardt) to the resultant potential energy curves. The procedure used for fitting dihedrals is identical to the standard method used within OPLS force-field development; namely, fitting the dihedral Fourier

coefficients to the difference between the quantum chemistry potential for the dihedral rotation and the force-field potential obtained by performing an optimized dihedral scan and summing all force-field contributions except for the dihedral being fit.[18] Note, the latter optimized dihedral scan is performed using the force-field potential. This procedure avoids double counting bond, angle, electrostatic, and Lennard-Jones contributions to the dihedral rotation. Unlike the OPLS procedure, no effort was made to remove contributions from the V_4 dihedral coefficient. At this point in the procedure, Lennard-Jones parameters for the intramolecular interactions are not yet determined, so universal force-field (UFF) parameters were used as an approximation when initially fitting the dihedrals.[19] The dihedrals were fit sequentially in a randomized order, until all Fourier coefficients for all modes converged to within 0.01 kcal/mol. During subsequent steps in the force-field generation, when Lennard-Jones parameters and the partial charges are refined, the dihedral potentials are refit with these updated parameters using the same procedure.

3.3 Fitting Procedure for Lennard-Jones Parameters and Atomic Charges

Condensed-phase all-atom MD simulations were used to generate ensembles of single molecule and pair configurations for refining the partial charges and parametrizing the Lennard-Jones interactions. The force-field potential for these simulations consisted of the intramolecular modes obtained as described above, the approximate equilibrium CHELPG charges, and Lennard-Jones parameters from UFF.[19] Five types of condensed phase MD simulations were performed for each oligomer type: model oligomer only, model oligomer with Li^+, model oligomer with Cl^-, model oligomer with triflate, and model oligomer with TFSI. Three additional MD simulations were performed with PEO to generate Li^+-anion configurations: PEO model compound with LiCl, Li triflate, and LiTFSI. The MD simulations were initialized with 30 oligomers placed randomly on a cubic lattice to avoid atomic overlaps. In simulations including ions, the ions were also added to sites on a cubic lattice, to reach a concentration of 1:20 ions per oligomer repeat unit. The initial coordinates were then rescaled to obtain a number density of 0.1 atoms·Å^{-3} (used as an approximate liquid density) and the charges on all atoms were scaled by 0.5 to reduce viscosity and accelerate configurational sampling. A one femtosecond timestep was used for all simulations. A uniform background charge was used to establish charge neutrality in simulations where only one species of ion was present. The remainder of the MD simulation details match those used in the rest of this work. The initial geometry was relaxed by performing 1 ps of NVE dynamics with atom displacements limited to 0.01 Å for each timestep, followed by 500 ps of NVT dynamics at a temperature of 400 K and pressure of 1 atm. After relaxation, an additional 2 ns of NVT dynamics were performed to collect production data used for generating single molecule and pair configurations used in the refinement of partial charges and calculation of Lennard-Jones parameters.

To refine the partial charges, one hundred molecular configurations for each model compound were sampled from the condensed phase simulations. Snapshots were drawn every 10 ps from the production data and the molecular coordinates were unwrapped to account for periodic boundary conditions. Snapshots were drawn until 100 molecular configurations had been parsed. For each parsed configuration, the DFT-calculated electron densities were used for CHELPG calculations to obtain nuclear charges. The atomic charges averaged across all configurations were used as the final charges in all simulations and also during the fitting of Lennard-Jones parameters (described below).

Configurations involving pairs of molecules were parsed from the condensed phase MD simulations for use in parametrizing the Lennard-Jones interactions. When sampling pair configurations from the condensed phase MD simulations, the following algorithm was used to ensure samples were included at short pairwise separations for all interactions being fit. Snapshots were drawn

every 10 ps from the production data and the molecular coordinates were unwrapped to account for periodic boundary conditions. In every snapshot there are many possible pairs of molecules, most of which occur at large separations and are not useful for fitting the binding and repulsive regions of the Lennard-Jones potential. A molecular pair was retained if at least one pair of atoms from each molecule resided within $r_{\text{thresh}} = 1.5\sigma_{ij}$, where σ_{ij} is the UFF Lennard-Jones radial parameter for the pair. Pairs of molecules were drawn this way until each pair of intermolecular atom types had at least 100 configurations within r_{thresh}. Once a given pair of atom types have at least 100 configurations within r_{thresh}, the pairwise separation of these atom types is no longer used as a criterion for keeping configurations. Usually this algorithm terminates after about 200 pairs of molecules are extracted from 1 ns of snapshots.

Counterpoise-corrected interaction energies, $E_{\text{I,DFT}}$, calculated for the pair of molecules, A and B, in each configuration were used to parametrize the Lennard-Jones interactions. $E_{\text{I,DFT}}$ was calculated according to

$$E_{\text{I,DFT}} = E_{\text{AB}}^{\text{AB}} - E_{\text{A}}^{\text{AB}} - E_{\text{B}}^{\text{AB}}, \tag{15}$$

where each term on the right-hand side corresponds to a single-point energy, the subscript of each term refers the atoms present in the calculation, and the superscript refers to the basis functions present in the calculation. In the context of the force-field, the interaction energy between molecules A and B, $E_{\text{I,FF}}$, is calculated as

$$E_{\text{I,FF}} = \sum_{i\in\text{A}}^{N_{\text{A}}} \sum_{j\in\text{B}}^{N_{\text{B}}} \left\{ \frac{q_i q_j e^2}{4\pi\epsilon_0 r_{ij}} + 4\epsilon_{ij} \left[\left(\frac{\sigma_{ij}}{r_{ij}} \right)^{12} - \left(\frac{\sigma_{ij}}{r_{ij}} \right)^{6} \right] \right\}, \tag{16}$$

where the summations run over the atoms on each molecule, q is the partial charge on each atom, and ϵ and σ are the Lennard-Jones parameters being fit. The Lennard-Jones parameters were obtained by performing numerical least-squares fitting (Levenberg-Marquardt) of $E_{\text{I,FF}}$ to $E_{\text{I,DFT}}$ across all pair configurations. The Lennard-Jones parameters for each pair type were iteratively fit until the variance converged to within 10^{-5} kcal/mol. UFF parameters were used as the starting guess for the fit, and in each iterative cycle the sequence of pair types was fit in a randomized order.

For polymer-polymer Lennard-Jones interactions, the above procedure yields all-atom Lennard-Jones parameters that accurately reproduce both the DFT-D3 interaction energies (section 6) and the experimental mass density of PEO (section 3). To obtain united-atom (UA) Lennard-Jones parameters from these values, each carbon atom and its attached hydrogens was refit as a single UA particle centered at the carbon atom to reproduce the all-atom (AA) Lennard-Jones potential. Further refinement of the UA parameters was performed to ensure that the UA-description reproduces the AA mass density and cohesive energy density (defined in the context of the force-field as the energy per unit volume of all Lennard-Jones interactions). This refinement was accomplished by running additional condensed phase simulations with uniform scaling of all UA-parameters. The scaling parameter for UA-ϵ values ranged from 0.5 to 1.0 in steps of 0.05. The scaling parameter for UA-σ values ranged from 1.0 to 1.3 in steps of 0.05. These simulations were initialized and run with the same protocol as described above, except with 50 oligomers in each simulation and unscaled partial charges. The initial geometry was relaxed by performing 1 ps of NVE dynamics with atom displacements limited to 0.01 Å for each timestep, followed by 250 ps of NPT dynamics at a temperature of 400 K and pressure of 1 atm. After relaxation, an additional 750 ps of NPT dynamics were performed to collect production data used for calculating the average mass and cohesive energy densities. The final UA-parameters were obtained by applying the combination of ϵ and σ scaling values which best reproduced the AA mass and cohesive energy densities.

For the polymer-ion Lennard-Jones interactions, the UA parameters were obtained by least-squares fitting of $E_{\mathrm{I,FF}}$ to $E_{\mathrm{I,DFT}}$ while excluding electrostatic and Lennard-Jones interactions between hydrogens attached to carbon and the ion (The fit results are presented in Section 6).

4 Force-Field Validation for PEO

Since no experimental data exists for the Lewis-acidic polymers, the approach developed here was to derive all force-field parameters directly from dispersion-corrected DFT calculations so that all polymers were represented at the same level of theory. PEO has been widely characterized and provides a basis for validating the force-field developed in this work. The average mass density of neat PEO at 400 K in the presented MD simulations is 0.994 $g \cdot cm^{-3}$, in good agreement with previously reported experimental and theoretical values.[20–22] The dilute ion concentration diffusivities for Li^+ and TFSI in PEO also show excellent agreement with NMR-based diffusivity measurements at dilute concentrations (Table S2).[23] The qualitative features of the dilute-ion coordination structure of Li^+ in PEO also agree well with the coordination structures observed in crystal structures of PEO oligomers with various Li^+ salts. Although crystal structures only exist for small oligomers of PEO at high salt concentrations, a common feature of these structures is coordination of Li^+ by four to five PEO oxygens, usually from a single chain, with the remaining one to two coordination positions occupied by anions.[24–26] In the presented MD simulations, Li^+ is tightly coordinated by four PEO oxygen atoms in the equatorial positions, and more weakly coordinated by two additional PEO oxygen atoms in the axial positions (Fig. 2a). In addition, the position and height of the first peak in the Li^+-polymer radial-distribution function agrees well with $g(r)$ obtained with other PEO force-fields (Fig. S1).[2,27] We also note that force-fields of this type employed here have been used to accurately simulate the relative Li-salt conductivity in PEO versus a range of polyester[3] and polyether[28] electrolytes.

In general, finite ion concentration MD simulations are less accurate than dilute ion concentration due to the importance of electronic polarization effects. As seen in Table S2, comparison of our simulations with available experiments at similar concentrations reveals excellent agreement for the LiTriflate salt, overestimation for the LiTFSI salt, and underestimation for the LiCl salt. These results are reasonably encouraging, as polarizable MD force fields that quantitatively reproduce finite-concentration PEO:LiTFSI diffusivities were parameterized against experimental diffusivity data,[29,30] which is not possible for the current study, as the proposed Lewis-acidic polymers have not yet been synthesized. Regardless, none of the main conclusions of this work are based on the absolute simulated conductivities of the polymer electrolytes in the finite-concentration regime.

Table S2: Comparison of experimental and simulated results for PEO at finite concentrations.[†]

Salt	Li:O	$\sigma_{\text{exp}}\,(\text{mS}\cdot\text{cm}^{-1})$	Avg. $\sigma_{\text{exp}}\,(\text{mS}\cdot\text{cm}^{-1})^{\ddagger}$	$\sigma_{\text{sim}}\,(\text{mS}\cdot\text{cm}^{-1})^{+}$
LiTFSI	1 : 10	2.0,[a] 1.0,[b] 0.63,[c] 1.0[d]	1.3 ± 0.4	0.11 ± 0.01
LiTFSI	1 : 20	2.0,[e] 1.2,[f] 0.85[g]	1.4 ± 0.3	0.05 ± 0.02
LiTriflate	1 : 10	0.002,[h] 0.1[i]	0.051 ± 0.05	0.03 ± 0.004
LiTriflate	1 : 20	0.06,[j] 0.08,[k] 0.2[l]	0.11 ± 0.04	0.07 ± 0.01
LiCl	1 : 10	-	-	0.07 ± 0.01
LiCl	1 : 20	0.002,[m] 0.003[n]	0.0025 ± 0.0005	0.09 ± 0.01

[†]For the dilute-ion regime, the simulated diffusivities ($7.9 \times 10^{-8}\,\text{cm}^2\cdot\text{s}^{-1}$ for Li^+ and $5.9 \times 10^{-7}\text{cm}^2\cdot\text{s}^{-1}$) for TFSI show good agreement with NMR-based diffusivity measurements at similar temperatures and at dilute concentrations ($7 - 9 \times 10^{-8}\text{cm}^2\cdot\text{s}^{-1}$ for Li^+ and $4 - 5 \times 10^{-7}\text{cm}^2\cdot\text{s}^{-1}$ for TFSI).
[‡]Standard errors among the various experimental reports.
[+]Standard errors from the simulation data.
[a]Lascaud et al. Macromolecules (1994) vol. 27 pp. 7469-7477 (1:11; 100C)
[b]Marzantowicz et al. J. Power Sources (2006) vol. 159 pp. 420-430 (1:10; 80C)
[c]Marzantowicz et al. J. Power Sources (2006) vol. 159 pp. 420-430 (1:12; 80C)
[d]Kim et al. (2007) vol. 171 pp. 861-869 (1:10; 100C)
[e]Lascaud et al. Macromolecules (1994) vol. 27 pp. 7469-7477 (1:24; 100C)
[f]Marzantowicz et al. J. Power Sources (2006) vol. 159 pp. 420-430 (1:16; 80C)
[g]Shin et al. Electrochem. Comm. (2003) vol. 5 pp. 1016-1020 (1:20; 90C)
[h]Walker and Salomon. J. Electrochem. Soc. (1993) vol. 140 pp. 3409-3412 (1:11; 74C)
[i]Caruso et al. Ionics (2002) vol. 8 pp. 36-43 (1:10; 103C)
[j]Walker and Salomon. J. Electrochem. Soc. (1993) vol. 140 pp. 3409-3412 (1:20; 74C)
[k]Fan et al. Solid State Ionics (2008) vol. 179 (27-32) pp. 1772-1775 (1:16; 80 C)
[l]Caruso et al. Ionics (2002) vol. 8 pp. 36-43 (1:20; 103C)
[m]Fan et al. Solid State Ionics (2008) vol. 179 (27-32) pp. 1772-1775 (1:16; 80 C)
[n]Watanabe et al. Macromolecules (1987) vol. 20 (3) pp. 569-573 (1:50, 75 C)

5 Force-Field Parameter Tables

5.1 Syntax for Defining Atom Types

Following the TAFFI protocol, unique atom types were determined on the basis of topological uniqueness out to two bonds. Here topology refers to the chemical bond connectivity graph (or adjacency matrix) of each model compound. Thus, each atom type reflects the local chemical structure of the atom out to two connected atoms. A simple syntax was developed for naming atom types, such that the name encodes the chemical connectivity about the atom type. In this syntax, all numbers refer to atomic numbers (i.e. 1 corresponds to hydrogen, and 6 to carbon), open brackets ("[") designate bonds, and closed brackets "]") designate the end of bonded groups (i.e. either the point at which two bonds is reached or at which a branch terminates). The central atom is always designated first, and descriptive notes are appended at the end of the label after a hyphen. As a rule, "[" implies a bond between the atom directly following the open bracket and the first atom preceding the bracket that is not enclosed by a "]". A canonicalization procedure is used to order the groups attached to the central atom so that the atom types are consistently generated. Several examples are illustrated in Fig. S4 for the model compound used to parametrize PEO.

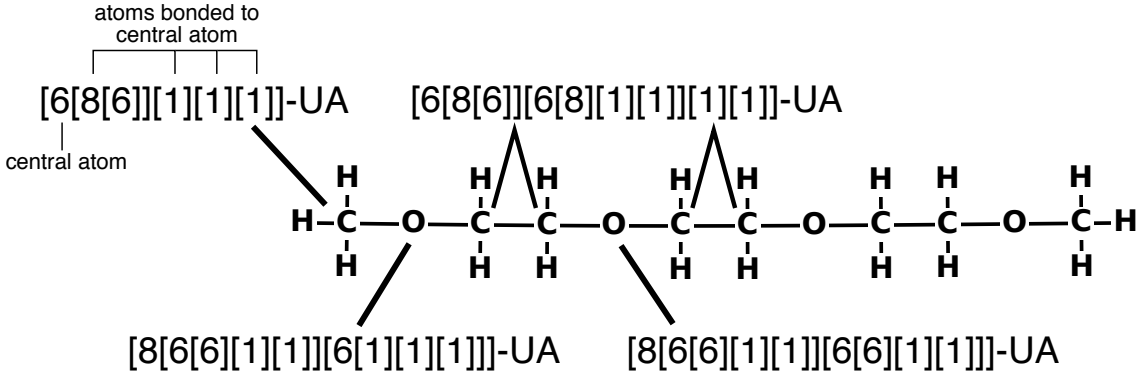

Figure S4: The model compound used for PEO parametrization, with several atom types shown as illustrations of the naming syntax.

5.2 PEO Parameter Tables

Table S3: Atomic parameters for PEO simulations.

Atom	Label	m (amu)	q (e)
[16[8][8][7[16]][6[9][9][9]]]-UA	S2	32.0660	1.0734
[16[8][8][8][6[9][9][9]]]-UA	S1	32.0660	1.1193
[17]-UA	Cl1	35.4527	-1.0000
[3]-UA	Li1	6.9410	1.0000
[6[16[8][8][7]][9][9][9]]-UA	C2	12.0110	0.3305
[6[16[8][8][8]][9][9][9]]-UA	C3	12.0110	0.4405
[6[8[6]][1][1][1]]-UA	C1	15.0348	0.1388
[6[8[6]][6[8][1][1]][1][1]]-UA	C4	14.0269	0.2268
[7[16[8][8][6]][16[8][8][6]]]-UA	N1	14.0067	-0.6816
[8[16[8][7][6]]]-UA	O3	15.9994	-0.5419
[8[16[8][8][6]]]-UA	O2	15.9994	-0.6365
[8[6[6][1][1]][6[1][1][1]]]-UA	O4	15.9994	-0.3582
[8[6[6][1][1]][6[6][1][1]]]-UA	O1	15.9994	-0.4609
[9[6[16][9][9]]]-UA-TFSI	F1	18.9984	-0.1598
[9[6[16][9][9]]]-UA-Triflate	F2	18.9984	-0.2168

Table S4: Lennard-Jones parameters for PEO simulations.

Pair[a]	σ_{ij} (Å)	ϵ_{ij} ($\frac{\text{kcal}}{\text{mol}}$)	Pair[a]	σ_{ij} (Å)	ϵ_{ij} ($\frac{\text{kcal}}{\text{mol}}$)	Pair[a]	σ_{ij} (Å)	ϵ_{ij} ($\frac{\text{kcal}}{\text{mol}}$)
C1-C1	0.1050	3.4309	F2-C4	0.0037	4.1811	O2-C3	0.0794	3.2745
C1-C2	0.3245	3.7074	F2-O1	0.2906	2.7786	O2-C4	0.0380	3.5338
C1-C3	0.2173	3.9166	F2-O2	0.0548	3.0576	O2-O2	0.0600	3.1181
C1-Cl1	3.4930	3.2303	F2-O4	0.0010	2.3633	O2-S1	0.1282	3.3565
C1-Li1	5.5726	2.4693	N1-C1	0.1738	3.0196	O3-C1	0.3640	3.1295
C1-S1	1.0738	3.6172	N1-C4	0.1539	3.1265	O3-C4	0.0114	3.9946
C1-S2	0.9863	3.6813	O1-C1	0.0508	4.0347	O4-C1	0.1164	3.7229
C4-C1	0.0010	3.3441	O1-C2	0.0804	3.9046	O4-C2	0.0010	2.8557
C4-C2	0.0091	4.8131	O1-C3	0.3810	2.8886	O4-C3	0.0176	4.5403
C4-C3	0.0825	3.1519	O1-C4	0.0173	4.4575	O4-C4	0.0227	4.3256
C4-C4	0.1525	4.1531	O1-Cl1	5.1649	3.2066	O4-Cl1	1.9051	3.2246
C4-Cl1	0.0083	4.8810	O1-Li1	0.0322	2.0532	O4-Li1	3.1720	1.8324
C4-Li1	4.1481	2.5062	O1-N1	0.7780	3.5464	O4-N1	0.0010	2.9674
C4-S1	0.1102	4.2195	O1-O1	1.6197	3.0194	O4-O2	0.2357	2.7715
C4-S2	0.0181	4.4415	O1-O2	0.0861	3.0885	O4-O3	0.4906	2.8529
F1-C1	0.1276	3.1589	O1-O3	0.6737	2.7089	O4-O4	0.7662	3.0684
F1-C4	0.0898	3.2350	O1-O4	0.7997	3.1961	O4-S1	0.3330	3.8991
F1-O1	0.0613	2.8028	O1-S1	2.9729	3.5470	O4-S2	0.0073	4.3930
F1-O4	0.0458	2.8172	O1-S2	1.0563	3.5549			
F2-C1	0.4454	3.0096	O2-C1	0.9280	2.9608			

[a]Atom types correspond to the labels in Table S3.

Table S5: Intramolecular parameters for PEO simulations.

Bond[a]	$k\,(\frac{\text{kcal}}{\text{mol}})$	r_0 (Å)	Angle[a]	$k\,(\frac{\text{kcal}}{\text{mol}})$	θ_0 (degrees)	Dihedral[a]	$V_1\,(\frac{\text{kcal}}{\text{mol}})$	$V_2\,(\frac{\text{kcal}}{\text{mol}})$	$V_3\,(\frac{\text{kcal}}{\text{mol}})$	$V_4\,(\frac{\text{kcal}}{\text{mol}})$
C1-O4	348.3839	1.4174	C1-O4-C4	75.1630	112.9953	C1-O4-C4-C4	5.1700	-1.9363	2.2300	-0.0080
C4-C4	312.0003	1.5208	C4-C4-O1	82.6123	107.8300	C4-C4-O1-C4	3.8612	-1.8428	2.4516	0.3515
C4-O1	340.9891	1.4198	C4-C4-O4	82.3129	107.8526	O1-C4-C4-O1	3.6952	-1.6906	1.8441	-0.0951
C4-O4	340.8649	1.4190	C4-O1-C4	72.7345	113.3741	O4-C4-C4-O1	6.3943	-3.3187	3.6780	-0.2097

[a]Atom types correspond to the labels in Table S3.

5.3 CBC Parameter Tables

Table S6: Atomic parameters for CBC simulations.

Atom	Label	m (amu)	q (e)
[16[8][8][7[16]][6[9][9][9]]]-UA	S2	32.0660	1.0734
[16[8][8][8][6[9][9][9]]]-UA	S1	32.0660	1.1193
[17]-UA	Cl1	35.4527	-1.0000
[3]-UA	Li1	6.9410	1.0000
[5[6[5][1][1]][6[1][1][1]][6[1][1][1]]]-UA	B1	10.8110	0.9347
[5[6[5][1][1]][6[5][1][1]][6[1][1][1]]]-UA	B2	10.8110	1.0316
[6[16[8][8][7]][9][9][9]]-UA	C3	12.0110	0.3305
[6[16[8][8][8]][9][9][9]]-UA	C4	12.0110	0.4405
[6[5[6][6]][1][1][1]]-UA	C2	15.0348	-0.3104
[6[5[6][6]][5[6][6]][1][1]]-UA	C1	14.0269	-0.6902
[7[16[8][8][6]][16[8][8][6]]]-UA	N1	14.0067	-0.6816
[8[16[8][7][6]]]-UA	O1	15.9994	-0.5419
[8[16[8][8][6]]]-UA	O2	15.9994	-0.6365
[9[6[16][9][9]]]-UA-TFSI	F1	18.9984	-0.1598
[9[6[16][9][9]]]-UA-Triflate	F2	18.9984	-0.2168

Table S7: Lennard-Jones parameters for CBC simulations.

Pair[a]	σ_{ij} (Å)	ϵ_{ij} ($\frac{\text{kcal}}{\text{mol}}$)	Pair[a]	σ_{ij} (Å)	ϵ_{ij} ($\frac{\text{kcal}}{\text{mol}}$)	Pair[a]	σ_{ij} (Å)	ϵ_{ij} ($\frac{\text{kcal}}{\text{mol}}$)
B1-B1	0.1800	3.6375	C1-S2	1.5341	3.2089	F2-C1	0.1846	3.2622
B1-Cl1	2.1494	3.7056	C2-B1	0.1378	3.7594	F2-C2	0.1773	2.9681
B1-Li1	7.7148	2.4555	C2-B2	0.3389	3.3056	F2-O2	0.0548	3.0576
B1-S1	0.0566	4.8106	C2-C2	0.1152	4.2112	N1-B1	1.9087	4.0343
B1-S2	0.0027	5.9711	C2-C3	0.0010	5.0515	N1-B2	0.0010	3.5344
B2-B1	0.1800	3.6375	C2-C4	0.0204	4.6323	N1-C1	0.0046	5.3217
B2-B2	0.1800	3.6375	C2-Cl1	0.3002	3.4605	N1-C2	1.1785	3.1062
B2-Cl1	0.0080	5.5014	C2-Li1	8.7889	2.3395	O1-B1	0.0010	2.6050
B2-Li1	13.5800	2.5708	C2-S1	1.0745	3.0204	O1-B2	0.0027	5.2539
B2-S1	0.0053	6.4735	C2-S2	0.1497	3.1051	O1-C1	0.8599	2.7148
B2-S2	0.0010	3.3453	C3-B1	0.0191	5.1728	O1-C2	0.0983	3.5500
C1-B1	0.1980	3.7806	C3-B2	0.0030	6.1934	O2-B1	0.0195	4.0466
C1-B2	0.0015	3.5184	C4-B1	0.1331	4.3235	O2-B2	0.0032	4.9278
C1-C1	0.1958	4.2512	C4-B2	0.0010	3.4872	O2-C1	1.7320	2.6593
C1-C2	0.1375	4.2031	F1-B1	0.4093	2.5297	O2-C2	0.1841	3.2994
C1-C3	0.1907	3.1642	F1-B2	0.0010	2.5059	O2-C4	0.0794	3.2745
C1-C4	0.0010	3.2949	F1-C1	0.4398	2.8530	O2-O2	0.0600	3.1181
C1-Cl1	3.4518	3.0169	F1-C2	0.0263	3.5359	O2-S1	0.1282	3.3565
C1-Li1	0.3445	2.9025	F2-B1	0.4131	3.0402			
C1-S1	2.7894	3.3492	F2-B2	0.0014	5.1073			

[a]Atom types correspond to the labels in Table S6.

Table S8: Intramolecular parameters for CBC simulations.

Bond[a]	$k\,(\frac{\text{kcal}}{\text{mol}})$	r_0 (Å)	Angle[a]	$k\,(\frac{\text{kcal}}{\text{mol}})$	θ_0 (degrees)	Dihedral[a]	$V_1\,(\frac{\text{kcal}}{\text{mol}})$	$V_2\,(\frac{\text{kcal}}{\text{mol}})$	$V_3\,(\frac{\text{kcal}}{\text{mol}})$	$V_4\,(\frac{\text{kcal}}{\text{mol}})$
B1-C1	232.3056	1.5790	B1-C1-B2	33.1351	113.3530	B1-C1-B2-C1	-13.3074	0.9454	0.8903	-1.5044
B1-C2	254.7037	1.5791	B2-C1-B2	25.7782	110.4320	B1-C1-B2-C2	-7.2348	-3.3289	0.7736	1.4828
B2-C1	213.3887	1.5837	C1-B2-C1	70.0835	120.6234	B2-C1-B1-C2	-0.5730	-0.6788	-1.5664	0.4294
B2-C2	252.4856	1.5815	C2-B1-C1	63.2298	121.1550	B2-C1-B2-C1	-1.9851	0.8404	1.0914	-0.9601
			C2-B1-C2	61.1794	118.1474	B2-C1-B2-C2	0.6715	0.4757	-0.4933	0.2771
			C2-B2-C1	70.9508	119.8894					

[a]Atom types correspond to the labels in Table S6.

5.4 CBCC Parameter Tables

Table S9: Atomic parameters for CBCC simulations.

Atom	Label	m (amu)	q (e)
[16[8][8][7[16]][6[9][9][9]]]-UA	S2	32.0660	1.0734
[16[8][8][8][6[9][9][9]]]-UA	S1	32.0660	1.1193
[17]-UA	Cl1	35.4527	-1.0000
[3]-UA	Li1	6.9410	1.0000
[5[6[6][1][1]][6[1][1][1]][6[1][1][1]]]-UA	B2	10.8110	0.8301
[5[6[6][1][1]][6[6][1][1]][6[1][1][1]]]-UA	B1	10.8110	0.6118
[6[16[8][8][7]][9][9][9]]-UA	C3	12.0110	0.3305
[6[16[8][8][8]][9][9][9]]-UA	C4	12.0110	0.4405
[6[5[6][6]][1][1][1]]-UA	C2	15.0348	-0.3018
[6[6[5][1][1]][5[6][6]][1][1]]-UA	C1	14.0269	-0.1789
[7[16[8][8][6]][16[8][8][6]]]-UA	N1	14.0067	-0.6816
[8[16[8][7][6]]]-UA	O1	15.9994	-0.5419
[8[16[8][8][6]]]-UA	O2	15.9994	-0.6365
[9[6[16][9][9]]]-UA-TFSI	F1	18.9984	-0.1598
[9[6[16][9][9]]]-UA-Triflate	F2	18.9984	-0.2168

Table S10: Lennard-Jones parameters for CBCC simulations.

Pair[a]	σ_{ij} (Å)	ϵ_{ij} ($\frac{\text{kcal}}{\text{mol}}$)	Pair[a]	σ_{ij} (Å)	ϵ_{ij} ($\frac{\text{kcal}}{\text{mol}}$)	Pair[a]	σ_{ij} (Å)	ϵ_{ij} ($\frac{\text{kcal}}{\text{mol}}$)
B1-B1	0.1800	3.6375	C1-S2	0.1940	3.3082	F2-C1	0.1523	3.3348
B1-B2	0.1800	3.6375	C2-B1	0.0869	3.3963	F2-C2	0.1915	3.1735
B1-Cl1	0.0243	4.3578	C2-B2	0.0066	2.9822	F2-O2	0.0548	3.0576
B1-Li1	4.3317	2.9037	C2-C2	0.1604	3.5439	N1-B1	4.2256	4.1396
B1-S1	0.0086	5.4222	C2-C3	0.0892	4.1311	N1-B2	0.0010	3.7841
B1-S2	0.4785	4.0609	C2-C4	1.3947	3.2561	N1-C1	0.0010	3.5981
B2-B2	0.1800	3.6375	C2-Cl1	4.0613	2.9067	N1-C2	1.0536	3.4994
B2-Cl1	0.0010	2.8866	C2-Li1	5.2410	2.2158	O1-B1	0.0010	2.5974
B2-Li1	16.2933	2.6932	C2-S1	0.4521	3.5286	O1-B2	0.0015	5.6053
B2-S1	0.0051	5.6304	C2-S2	0.0054	5.0248	O1-C1	0.0045	4.3752
B2-S2	0.0010	3.3526	C3-B1	0.3975	3.9347	O1-C2	0.9469	2.5709
C1-B1	0.0738	3.2313	C3-B2	0.0010	3.2468	O2-B1	1.1865	3.0230
C1-B2	0.0803	3.0918	C4-B1	0.3365	3.3607	O2-B2	0.0016	5.0469
C1-C1	0.1397	3.4357	C4-B2	0.0010	3.3679	O2-C1	0.3076	3.3306
C1-C2	0.1421	3.5153	F1-B1	0.1973	3.5029	O2-C2	0.5208	3.0149
C1-C3	0.0010	5.9132	F1-B2	0.0010	4.9924	O2-C4	0.0794	3.2745
C1-C4	0.4283	3.3330	F1-C1	0.0012	4.3655	O2-O2	0.0600	3.1181
C1-Cl1	0.4599	3.7222	F1-C2	0.2200	3.1572	O2-S1	0.1282	3.3565
C1-Li1	11.1239	2.0295	F2-B1	0.0034	2.5879			
C1-S1	0.0106	4.7999	F2-B2	0.0013	5.2502			

[a]Atom types correspond to the labels in Table S9.

Table S11: Intramolecular parameters for CBCC simulations.

Bond[a]	k ($\frac{\text{kcal}}{\text{mol}}$)	r_0 (Å)	Angle[a]	k ($\frac{\text{kcal}}{\text{mol}}$)	θ_0 (degrees)	Dihedral[a]	V_1 ($\frac{\text{kcal}}{\text{mol}}$)	V_2 ($\frac{\text{kcal}}{\text{mol}}$)	V_3 ($\frac{\text{kcal}}{\text{mol}}$)	V_4 ($\frac{\text{kcal}}{\text{mol}}$)
B1-C1	248.2053	1.5828	B1-C1-C1	61.7531	118.6635	B1-C1-C1-B1	3.3239	3.7914	-0.8343	1.3696
B1-C2	256.0949	1.5754	B2-C1-C1	31.6742	106.7799	B2-C1-C1-B1	11.9121	1.8814	0.1416	0.9374
B2-C1	255.6278	1.5754	C1-B1-C1	66.4949	118.3454	C1-B1-C1-C1	-3.4483	2.2207	-3.2360	-0.1405
B2-C2	255.1161	1.5782	C2-B1-C1	61.5526	121.3437	C2-B1-C1-C1	6.8959	1.3393	-1.8685	1.8090
C1-C1	241.9187	1.5606	C2-B2-C1	59.7090	119.6654	C2-B2-C1-C1	2.2216	-0.0175	-0.2227	0.1320
			C2-B2-C2	49.2138	120.3698					

[a]Atom types correspond to the labels in Table S9.

5.5 HBC Parameter Tables

Table S12: Atomic parameters for HBC simulations.

Atom	Label	m (amu)	q (e)
[16[8][8][7[16]][6[9][9][9]]]-UA	S2	32.0660	1.0734
[16[8][8][8][6[9][9][9]]]-UA	S1	32.0660	1.1193
[17]-UA	Cl1	35.4527	-1.0000
[1[5[6][6]]]-UA	H1	1.0079	-0.2742
[3]-UA	Li1	6.9410	1.0000
[5[6[5][1][1]][6[1][1][1]][1]]-UA	B2	10.8110	0.8684
[5[6[5][1][1]][6[5][1][1]][1]]-UA	B1	10.8110	0.8593
[6[16[8][8][7]][9][9][9]]-UA	C2	12.0110	0.3305
[6[16[8][8][8]][9][9][9]]-UA	C3	12.0110	0.4405
[6[5[6][1]][1][1][1]]-UA	C1	15.0348	-0.2872
[6[5[6][1]][5[6][1]][1][1]]-UA	C4	14.0269	-0.5948
[7[16[8][8][6]][16[8][8][6]]]-UA	N1	14.0067	-0.6816
[8[16[8][7][6]]]-UA	O2	15.9994	-0.5419
[8[16[8][8][6]]]-UA	O1	15.9994	-0.6365
[9[6[16][9][9]]]-UA-TFSI	F1	18.9984	-0.1598
[9[6[16][9][9]]]-UA-Triflate	F2	18.9984	-0.2168

Table S13: Lennard-Jones parameters for HBC simulations.

Pair[a]	σ_{ij} (Å)	ϵ_{ij} ($\frac{\text{kcal}}{\text{mol}}$)	Pair[a]	σ_{ij} (Å)	ϵ_{ij} ($\frac{\text{kcal}}{\text{mol}}$)	Pair[a]	σ_{ij} (Å)	ϵ_{ij} ($\frac{\text{kcal}}{\text{mol}}$)
B1-B1	0.1800	3.6375	C2-H1	0.0010	2.6097	F2-O1	0.0548	3.0576
B1-B2	0.1800	3.6375	C3-B1	0.0014	6.6607	H1-Cl1	0.0010	2.3965
B1-Cl1	0.0066	5.4526	C3-B2	0.0010	3.1546	H1-H1	0.0440	2.5711
B1-H1	0.0890	3.1043	C3-H1	0.0010	2.5092	H1-S1	0.0010	2.6708
B1-Li1	5.2357	2.5866	C4-B1	0.0880	3.4416	H1-S2	0.0010	2.4544
B1-S1	0.0016	6.2420	C4-B2	0.2738	3.4931	Li1-H1	9.3292	1.8203
B1-S2	0.0010	3.1090	C4-C1	0.1243	4.2083	N1-B1	0.0010	3.3383
B2-B2	0.1800	3.6375	C4-C2	0.4016	3.2967	N1-B2	0.0010	3.0845
B2-Cl1	0.0010	2.8024	C4-C3	0.0801	4.2456	N1-C1	2.1688	3.4621
B2-H1	0.0890	3.1043	C4-C4	0.1224	4.2285	N1-C4	0.0010	3.3279
B2-Li1	10.4170	2.3764	C4-Cl1	6.5002	2.9389	N1-H1	0.0010	4.5661
B2-S1	0.0010	3.1439	C4-H1	0.0228	3.7824	O1-B1	0.0058	4.8692
B2-S2	0.0010	6.2627	C4-Li1	0.0010	4.3570	O1-B2	0.0024	5.0803
C1-B1	0.1902	3.8363	C4-S1	1.3978	3.2707	O1-C1	0.8426	2.5469
C1-B2	0.1819	3.5456	C4-S2	1.9654	3.1337	O1-C3	0.0794	3.2745
C1-C1	0.1591	4.0654	F1-B1	0.0031	4.6433	O1-C4	2.8442	2.7131
C1-C2	0.1130	3.0919	F1-B2	0.0031	4.5724	O1-H1	0.0010	2.1353
C1-C3	0.7992	3.3080	F1-C1	0.0117	3.7189	O1-O1	0.0600	3.1181
C1-Cl1	0.0195	3.9996	F1-C4	1.2762	2.5652	O1-S1	0.1282	3.3565
C1-H1	0.0257	3.7387	F1-H1	0.0040	3.4612	O2-B1	0.0018	5.1097
C1-Li1	7.8126	2.2888	F2-B1	0.0015	5.1739	O2-B2	0.0018	5.0999
C1-S1	0.0010	3.2338	F2-B2	0.0022	4.9205	O2-C1	0.4122	2.4934
C1-S2	0.0488	4.3837	F2-C1	0.0099	3.8456	O2-C4	1.7348	2.6048
C2-B1	0.0020	6.2445	F2-C4	2.6196	2.5479	O2-H1	0.0049	3.6638
C2-B2	0.0010	3.2214	F2-H1	0.0010	2.0402			

[a]Atom types correspond to the labels in Table S12.

Table S14: Intramolecular parameters for HBC simulations.

Bond[a]	$k\,(\frac{\text{kcal}}{\text{mol}})$	r_0 (Å)	Angle[a]	$k\,(\frac{\text{kcal}}{\text{mol}})$	θ_0 (degrees)	Dihedral[a]	$V_1\,(\frac{\text{kcal}}{\text{mol}})$	$V_2\,(\frac{\text{kcal}}{\text{mol}})$	$V_3\,(\frac{\text{kcal}}{\text{mol}})$	$V_4\,(\frac{\text{kcal}}{\text{mol}})$
B1-C4	241.3756	1.5705	B1-C4-B1	27.7807	106.7004	B1-C4-B1-C4	-3.9887	1.3337	-2.1262	0.4463
B2-C1	269.7731	1.5662	B2-C4-B1	24.7349	106.8924	B1-C4-B2-C1	0.1277	-0.9754	0.1200	-0.0160
B2-C4	240.6383	1.5708	C1-B2-C4	52.4693	123.2142	B2-C4-B1-C4	-2.6490	1.1176	-0.2814	-0.3637
H1-B1	262.2066	1.2030	C4-B1-C4	55.4532	122.5544	H1-B1-C4-B1	-2.4033	-1.6903	-0.9231	-1.6210
H1-B2	260.0591	1.2048	H1-B1-C4	48.1681	118.8050	H1-B1-C4-B2	2.5105	-2.4940	0.1429	0.2511
			H1-B2-C1	44.4883	118.3976	H1-B2-C4-B1	0.0147	-1.2149	0.2320	-0.4234
			H1-B2-C4	47.9228	118.5387					

[a]Atom types correspond to the labels in Table S12.

5.6 HBCC Parameter Tables

Table S15: Atomic parameters for HBCC simulations.

Atom	Label	m (amu)	q (e)
[16[8][8][7[16]][6[9][9][9]]]-UA	S2	32.0660	1.0734
[16[8][8][8][6[9][9][9]]]-UA	S1	32.0660	1.1193
[17]-UA	Cl1	35.4527	-1.0000
[1[5[6][6]]]-UA	H1	1.0079	-0.2641
[3]-UA	Li1	6.9410	1.0000
[5[6[6][1][1]][6[1][1][1]][1]]-UA	B2	10.8110	0.7760
[5[6[6][1][1]][6[6][1][1]][1]]-UA	B1	10.8110	0.6119
[6[16[8][8][7]][9][9][9]]-UA	C1	12.0110	0.3305
[6[16[8][8][8]][9][9][9]]-UA	C4	12.0110	0.4405
[6[5[6][1]][1][1][1]]-UA	C3	15.0348	-0.2780
[6[6[5][1][1]][5[6][1]][1][1]]-UA	C2	14.0269	-0.1939
[7[16[8][8][6]][16[8][8][6]]]-UA	N1	14.0067	-0.6816
[8[16[8][7][6]]]-UA	O2	15.9994	-0.5419
[8[16[8][8][6]]]-UA	O1	15.9994	-0.6365
[9[6[16][9][9]]]-UA-TFSI	F1	18.9984	-0.1598
[9[6[16][9][9]]]-UA-Triflate	F2	18.9984	-0.2168

Table S16: Lennard-Jones parameters for HBCC simulations.

Pair[a]	σ_{ij} (Å)	ϵ_{ij} ($\frac{\text{kcal}}{\text{mol}}$)	Pair[a]	σ_{ij} (Å)	ϵ_{ij} ($\frac{\text{kcal}}{\text{mol}}$)	Pair[a]	σ_{ij} (Å)	ϵ_{ij} ($\frac{\text{kcal}}{\text{mol}}$)
B1-B1	0.1800	3.6375	C2-S1	0.2937	3.6220	F2-O1	0.0548	3.0576
B1-B2	0.1800	3.6375	C2-S2	0.3637	3.6418	H1-Cl1	0.0018	3.9679
B1-Cl1	2.6935	2.8271	C3-B1	0.1923	3.1819	H1-H1	0.0440	2.5711
B1-H1	0.0890	3.1043	C3-B2	0.2003	3.4077	H1-S1	0.0010	2.7015
B1-Li1	7.7192	2.4021	C3-C1	0.2339	3.9721	H1-S2	0.0029	4.1673
B1-S1	0.0220	4.9485	C3-C3	0.1063	3.9380	Li1-H1	1.3246	1.9716
B1-S2	0.1297	3.9894	C3-C4	0.0040	5.4940	N1-B1	0.4727	3.5420
B2-B2	0.1800	3.6375	C3-Cl1	4.4564	3.1288	N1-B2	0.0010	3.3564
B2-Cl1	0.0319	4.5159	C3-H1	0.0106	3.6425	N1-C2	0.0015	5.0627
B2-H1	0.0890	3.1043	C3-Li1	2.0162	2.5613	N1-C3	1.1281	3.3460
B2-Li1	14.9347	2.5725	C3-S1	1.5755	3.2006	N1-H1	0.0010	2.7751
B2-S1	0.0020	6.4299	C3-S2	0.3795	3.9270	O1-B1	1.3836	2.5545
B2-S2	0.0010	3.1381	C4-B1	0.0636	4.5976	O1-B2	0.0037	4.6250
C1-B1	0.4179	3.8277	C4-B2	0.0010	5.8000	O1-C2	0.6207	3.2344
C1-B2	0.0010	3.3219	C4-H1	0.0010	2.7039	O1-C3	1.2335	2.9560
C1-H1	0.0010	2.7098	F1-B1	0.0167	2.9321	O1-C4	0.0794	3.2745
C2-B1	0.0496	3.1892	F1-B2	0.0026	4.5942	O1-H1	0.3336	2.0889
C2-B2	0.1606	3.2756	F1-C2	0.0910	3.3167	O1-O1	0.0600	3.1181
C2-C1	0.0010	3.2131	F1-C3	0.4699	2.9787	O1-S1	0.1282	3.3565
C2-C2	0.1819	3.8140	F1-H1	0.0024	3.5375	O2-B1	0.1752	2.4663
C2-C3	0.1282	3.8504	F2-B1	0.0057	3.5124	O2-B2	0.0047	4.6847
C2-C4	0.0311	3.8446	F2-B2	0.0013	4.8052	O2-C2	0.3657	3.1507
C2-Cl1	1.6421	3.3973	F2-C2	0.1965	3.2182	O2-C3	0.8674	2.8904
C2-H1	0.0744	3.2059	F2-C3	1.2285	2.8041	O2-H1	0.0010	2.0904
C2-Li1	3.0619	2.5572	F2-H1	0.0211	2.9542			

[a]Atom types correspond to the labels in Table S15.

Table S17: Intramolecular parameters for HBCC simulations.

Bond[a]	$k\,(\frac{\text{kcal}}{\text{mol}})$	r_0 (Å)	Angle[a]	$k\,(\frac{\text{kcal}}{\text{mol}})$	θ_0 (degrees)	Dihedral[a]	$V_1\,(\frac{\text{kcal}}{\text{mol}})$	$V_2\,(\frac{\text{kcal}}{\text{mol}})$	$V_3\,(\frac{\text{kcal}}{\text{mol}})$	$V_4\,(\frac{\text{kcal}}{\text{mol}})$
B1-C2	262.5299	1.5664	B1-C2-C2	38.6545	117.7502	B1-C2-C2-B1	10.3866	-0.6689	2.0740	0.0463
B2-C2	263.8729	1.5664	B2-C2-C2	44.3290	118.2331	B2-C2-C2-B1	13.9722	-1.5753	1.3512	0.2761
B2-C3	266.9141	1.5672	C2-B1-C2	47.9064	122.9635	C2-B1-C2-C2	0.3542	1.7026	-1.3785	-0.2549
C2-C2	287.7822	1.5422	C3-B2-C2	46.8288	122.9528	C3-B2-C2-C2	0.2337	0.3147	-0.1421	0.1065
H1-B1	253.2126	1.2093	H1-B1-C2	42.5869	118.6413	H1-B1-C2-C2	0.5861	1.6786	-0.0075	0.1503
H1-B2	255.8662	1.2077	H1-B2-C2	41.6971	118.8230	H1-B2-C2-C2	-0.2422	0.1767	0.1774	0.2636
			H1-B2-C3	43.6002	118.4065					

[a]Atom types correspond to the labels in Table S15.

5.7 Cl^- Parameter Tables

Table S18: Atomic parameters for Cl^- simulations

Atom	Label	m (amu)	q (e)
[17]-UA	Cl1	35.4527	-1.0000
[3]-UA	Li1	6.9410	1.0000

Table S19: Lennard-Jones parameters for Cl^- simulations.

Pair[a]	σ_{ij} (Å)	ϵ_{ij} ($\frac{\text{kcal}}{\text{mol}}$)
Cl1-Cl1	0.2270	3.5164
Li1-Cl1	9.2424	2.2822

[a]Atom types correspond to the labels in Table S18.

5.8 Triflate Parameter Tables

Table S20: Atomic parameters for triflate simulations

Atom	Label	m (amu)	q (e)
[16[8][8][8][6[9][9][9]]]-UA	S1	32.0660	1.1193
[6[16[8][8][8]][9][9][9]]-UA	C1	12.0110	0.4405
[8[16[8][8][6]]]-UA	O1	15.9994	-0.6365
[9[6[16][9][9]]]-UA	F1	18.9984	-0.2168
[3]-UA	Li1	6.9410	1.0000

Table S21: Lennard-Jones parameters for triflate simulations.

Pair[a]	σ_{ij} (Å)	ϵ_{ij} ($\frac{\text{kcal}}{\text{mol}}$)
C1-C1	0.1050	3.4309
C1-Li1	0.0180	3.7206
C1-S1	0.1696	3.5128
F1-C1	0.0725	3.2139
F1-F1	0.0500	2.9970
F1-Li1	5.7608	1.9488
F1-O1	0.0548	3.0576
F1-S1	0.1170	3.2959
Li1-S1	1.3957	2.7964
O1-C1	0.0794	3.2745
O1-Li1	8.4364	1.9425
O1-O1	0.0600	3.1181
O1-S1	0.1282	3.3565
S1-S1	0.2740	3.5948

[a]Atom types correspond to the labels in Table S20.

Table S22: Intramolecular parameters for triflate simulations.

Bond[a]	k ($\frac{\text{kcal}}{\text{mol}}$)	r_0 (Å)	Angle[a]	k ($\frac{\text{kcal}}{\text{mol}}$)	θ_0 (degrees)	Dihedral[a]	V_1 ($\frac{\text{kcal}}{\text{mol}}$)	V_2 ($\frac{\text{kcal}}{\text{mol}}$)	V_3 ($\frac{\text{kcal}}{\text{mol}}$)	V_4 ($\frac{\text{kcal}}{\text{mol}}$)
C2-F2	353.7506	1.3596	C2-S2-O2	88.6478	102.3759	O1-S1-C1-F1	-2.2268	-1.0401	0.4445	1.8495
S2-C2	172.0823	1.8760	F2-C2-F2	122.2029	106.8052					
S2-O2	671.4135	1.4607	O2-S2-O2	134.6661	115.6511					
			S2-C2-F2	76.0103	112.1533					

[a]Atom types correspond to the labels in Table S20.

5.9 TFSI- Parameter Tables

Table S23: Atomic parameters for TFSI- simulations

Atom	Label	m (amu)	q (e)
[16[8][8][7[16]][6[9][9][9]]]-UA	S2	32.0660	1.0734
[6[16[8][8][7]][9][9][9]]-UA	C1	12.0110	0.3305
[7[16[8][8][6]][16[8][8][6]]]-UA	N1	14.0067	-0.6816
[8[16[8][7][6]]]-UA	O1	15.9994	-0.5419
[9[6[16][9][9]]]-UA	F1	18.9984	-0.1598
[3]-UA	Li1	6.9410	1.0000

Table S24: Lennard-Jones parameters for TFSI- simulations.

Pair[a]	σ_{ij} (Å)	ϵ_{ij} ($\frac{\text{kcal}}{\text{mol}}$)
C1-C1	0.1050	3.4309
C1-Li1	9.0805	2.6855
C1-S2	0.1696	3.5128
F1-C1	0.0725	3.2139
F1-F1	0.0500	2.9970
F1-Li1	0.5683	1.7900
F1-N1	0.0587	3.1288
F1-O1	0.0548	3.0576
F1-S2	0.1170	3.2959
Li1-S2	0.5121	2.9625
N1-C1	0.0851	3.3458
N1-Li1	0.0010	2.2778
N1-N1	0.0690	3.2607
N1-S2	0.1375	3.4277
O1-C1	0.0794	3.2745
O1-Li1	7.6513	1.9299
O1-N1	0.0643	3.1894
O1-O1	0.0600	3.1181
O1-S2	0.1282	3.3565
S2-S2	0.2740	3.5948

[a]Atom types correspond to the labels in Table S23.

Table S25: Intramolecular parameters for TFSI- simulations.

Bond[a]	k ($\frac{\text{kcal}}{\text{mol}}$)	r_0 (Å)	Angle[a]	k ($\frac{\text{kcal}}{\text{mol}}$)	θ_0 (degrees)	Dihedral[a]	V_1 ($\frac{\text{kcal}}{\text{mol}}$)	V_2 ($\frac{\text{kcal}}{\text{mol}}$)	V_3 ($\frac{\text{kcal}}{\text{mol}}$)	V_4 ($\frac{\text{kcal}}{\text{mol}}$)
C2-F2	380.3657	1.3483	C2-S1-N2	70.1005	98.9717	N1-S2-C1-F1	3.1887	12.2415	1.2828	11.6296
S1-C2	182.3244	1.8731	C2-S1-O2	86.2016	103.3834	O1-S2-C1-F1	-1.8803	12.7720	-0.0974	12.7720
S1-N2	341.6037	1.5902	F2-C2-F2	120.4710	108.1211	O1-S2-N1-S2	-0.5300	-0.3077	-0.1853	2.0016
S1-O2	719.9940	1.4479	N2-S1-O2	91.7672	111.4256	S2-N1-S2-C1	13.1981	-0.3478	-1.8131	0.9827
			O2-S1-O2	120.7440	118.8719					
			S1-C2-F2	77.5978	111.7436					
			S1-N2-S1	47.4866	127.7101					

[a]Atom types correspond to the labels in Table S23.

6 Force-Field Fit Potentials: Bonds, Angles, Dihedrals

6.1 PEO Bond, Angle, and Dihedral Fits

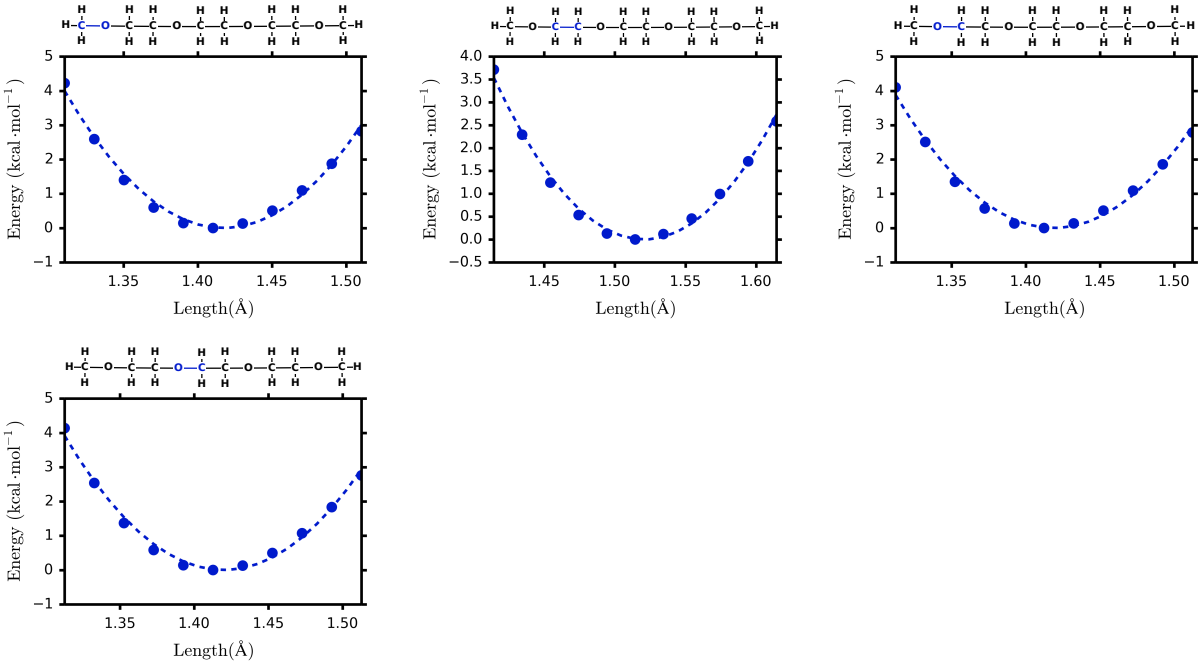

Figure S5: PEO bond potentials (blue dots) calculated at the B3LYP-D3/def2-TZVP level of theory, shown with harmonic fits (dotted lines). The energy minima have been set to zero.

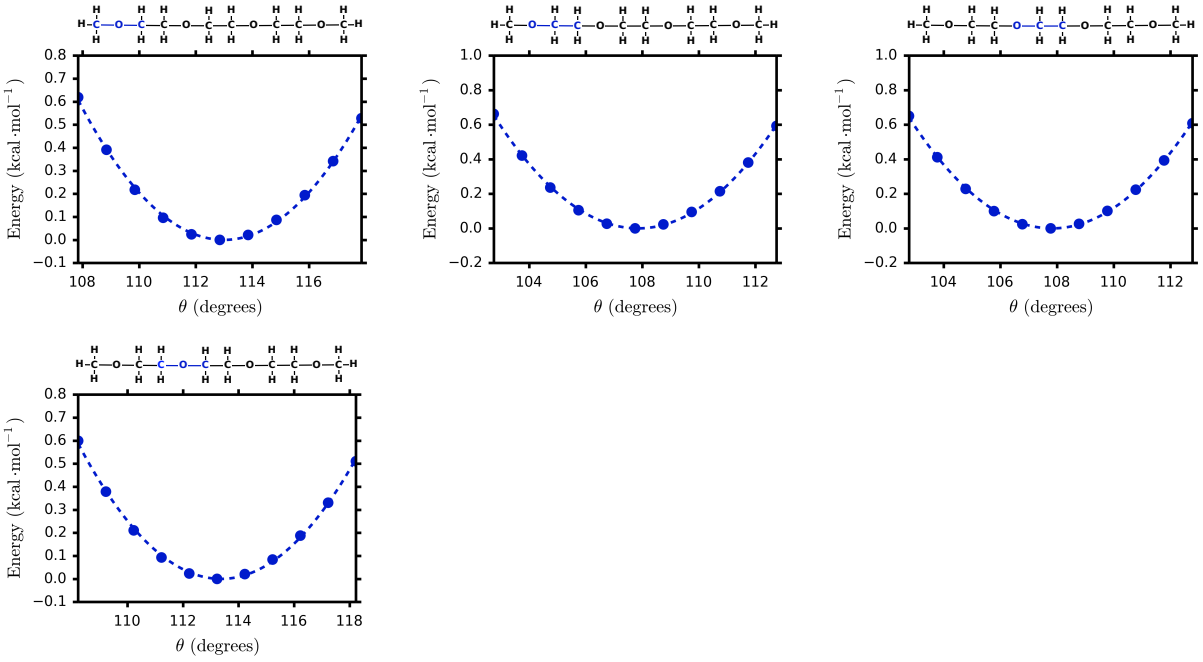

Figure S6: PEO angle potentials (blue dots) calculated at the B3LYP-D3/def2-TZVP level of theory, shown with harmonic fits (dotted lines). The energy minima have been set to zero.

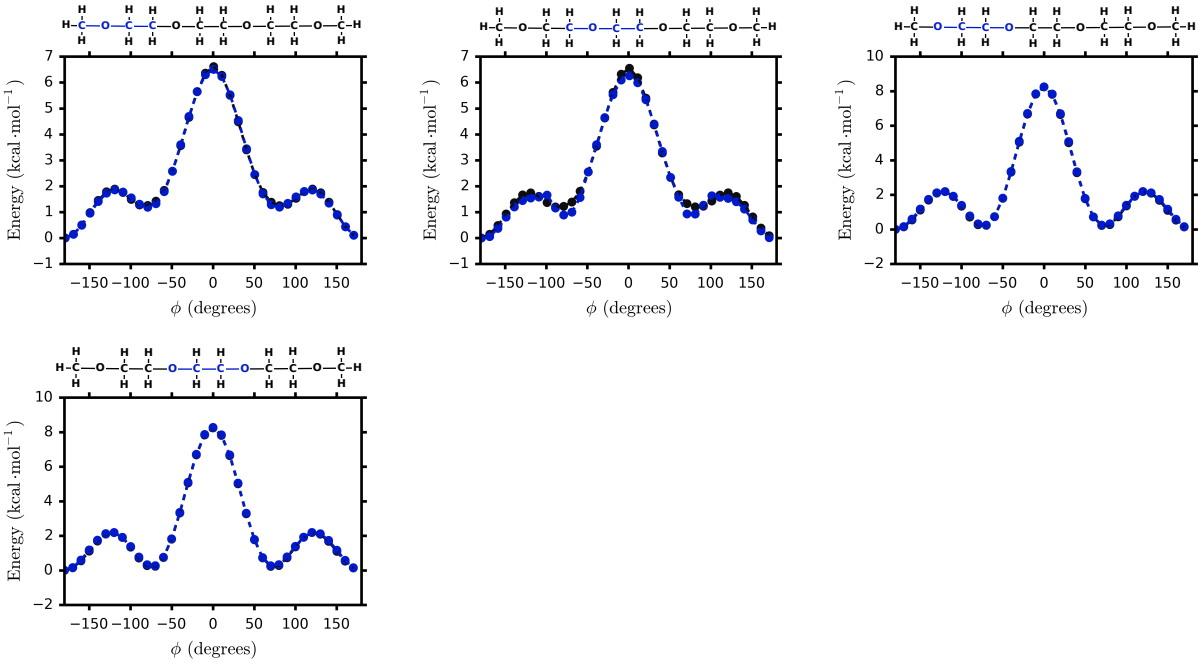

Figure S7: PEO dihedral potentials (black dots) calculated at the B3LYP-D3/def2-TZVP level of theory, shown with fits to the OPLS potential (blue dots). The configuration closest to -180° has been set to zero in each plot.

6.2 CBC Bond, Angle, and Dihedral Fits

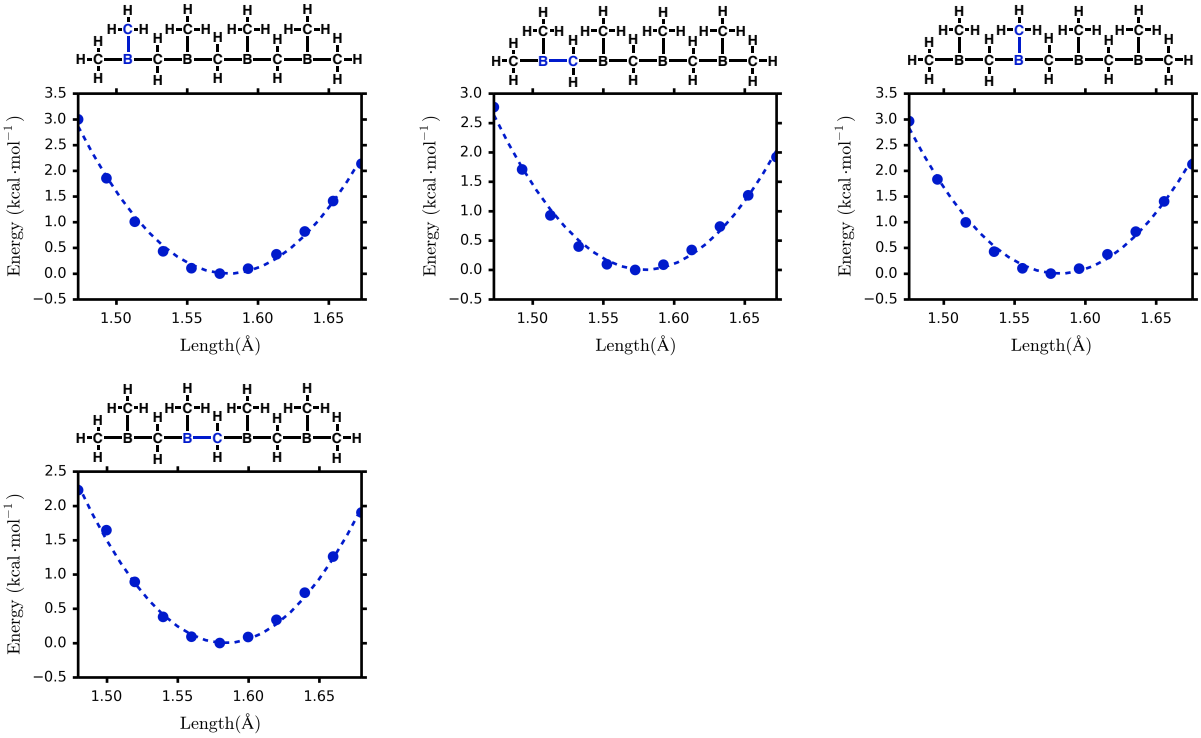

Figure S8: CBC bond potentials (blue dots) calculated at the B3LYP-D3/def2-TZVP level of theory, shown with harmonic fits (dotted lines). The energy minima have been set to zero.

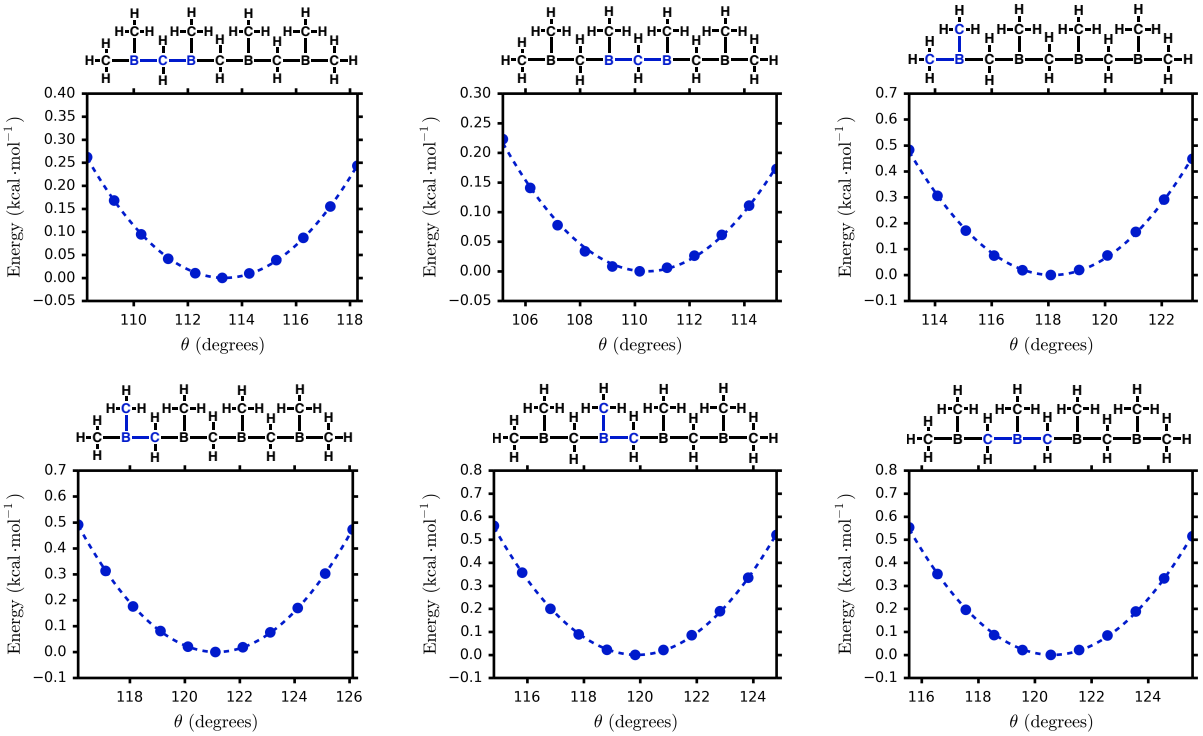

Figure S9: CBC angle potentials (blue dots) calculated at the B3LYP-D3/def2-TZVP level of theory, shown with harmonic fits (dotted lines). The energy minima have been set to zero.

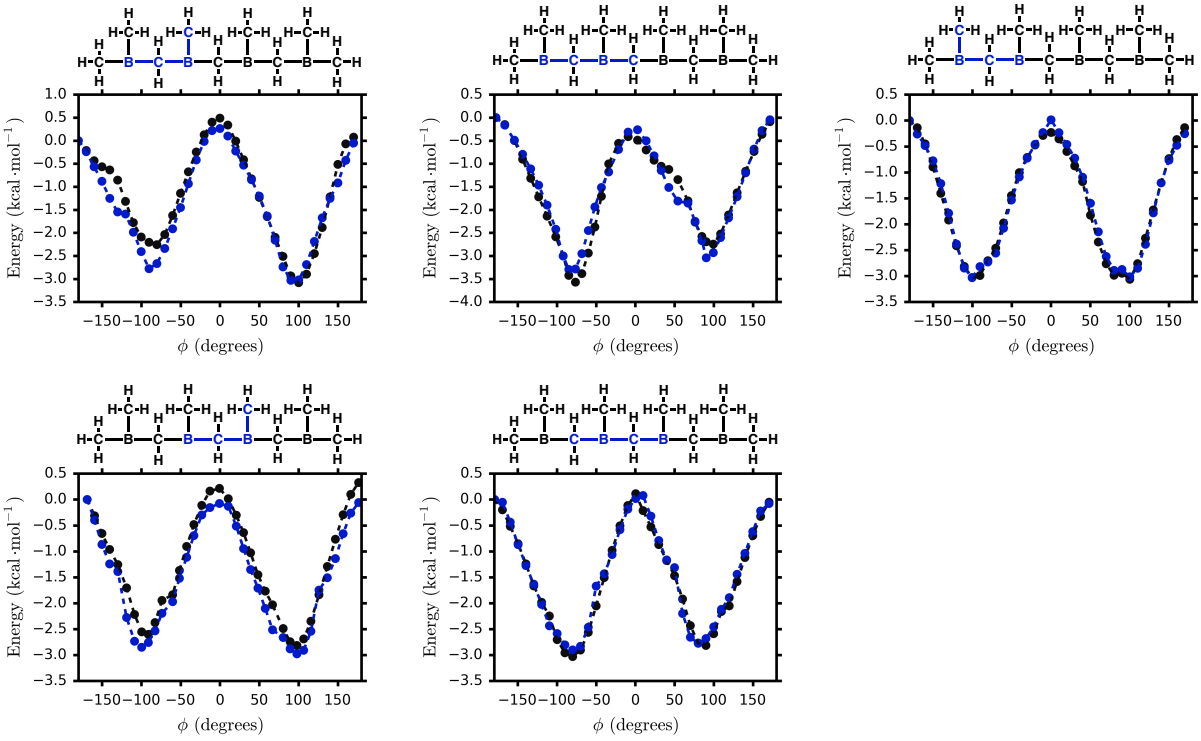

Figure S10: CBC dihedral potentials (black dots) calculated at the B3LYP-D3/def2-TZVP level of theory, shown with fits to the OPLS potential (blue dots). The configuration closest to -180° has been set to zero in each plot.

6.3 CBCC Bond, Angle, and Dihedral Fits

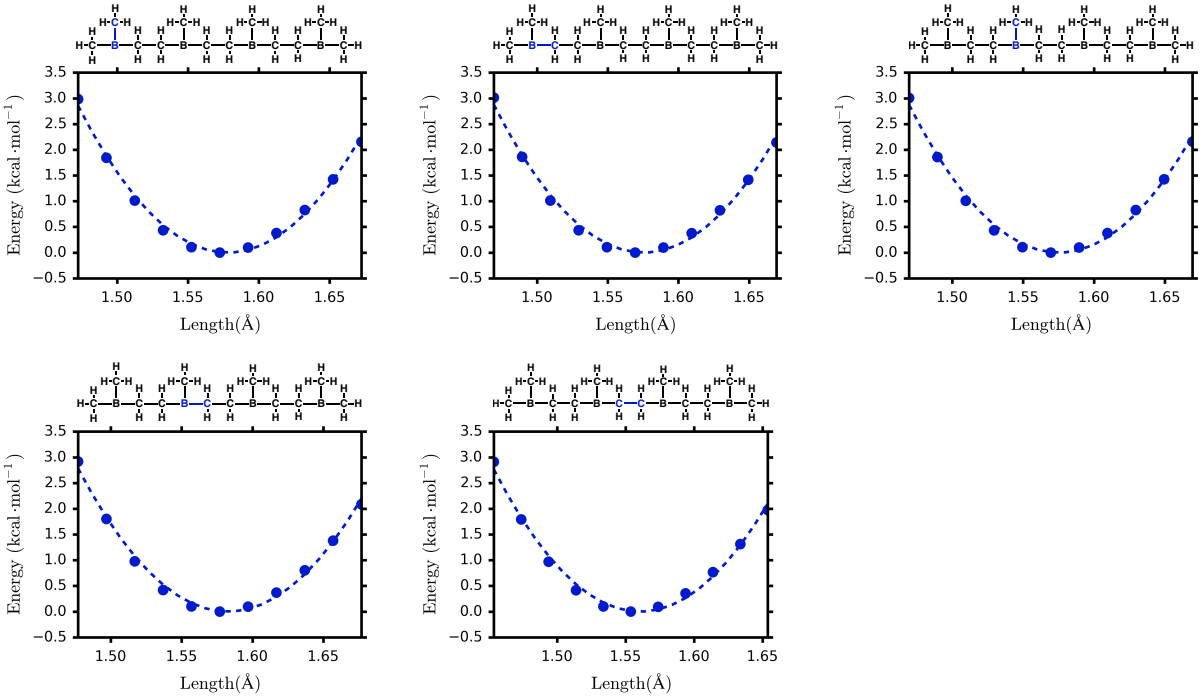

Figure S11: CBCC bond potentials (blue dots) calculated at the B3LYP-D3/def2-TZVP level of theory, shown with harmonic fits (dotted lines). The energy minima have been set to zero.

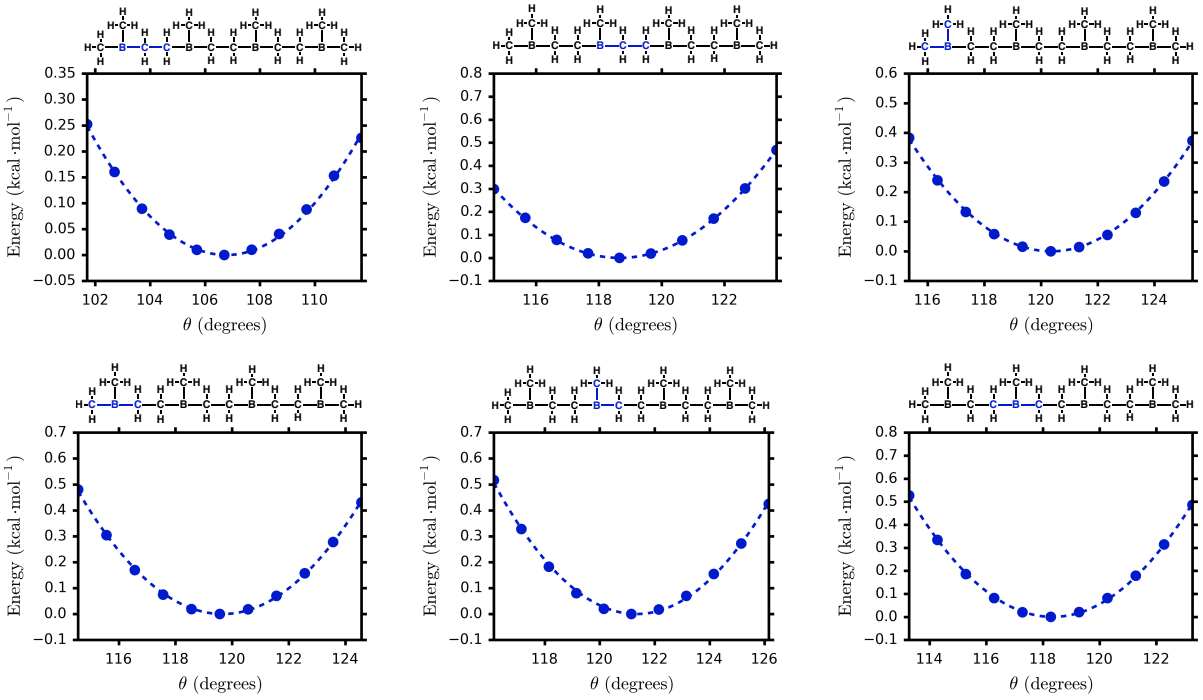

Figure S12: CBCC angle potentials (blue dots) calculated at the B3LYP-D3/def2-TZVP level of theory, shown with harmonic fits (dotted lines). The energy minima have been set to zero.

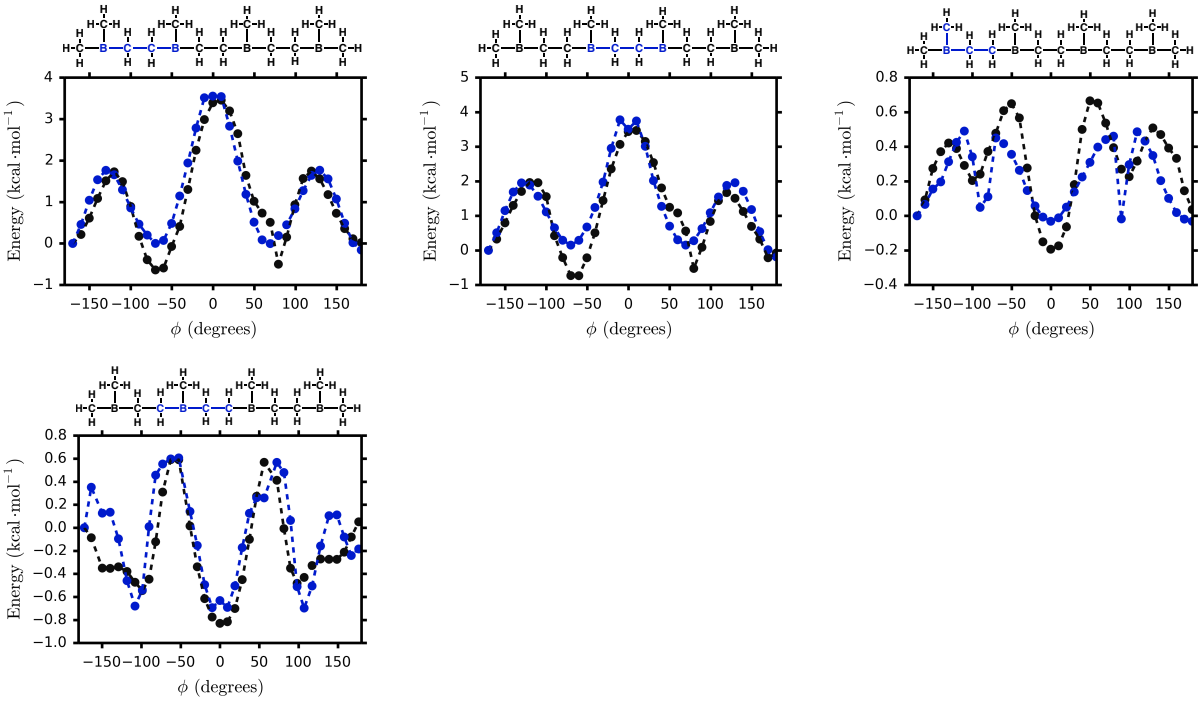

Figure S13: CBCC dihedral potentials (black dots) calculated at the B3LYP-D3/def2-TZVP level of theory, shown with fits to the OPLS potential (blue dots). The configuration closest to -180° has been set to zero in each plot.

6.4 HBC Bond, Angle, and Dihedral Fits

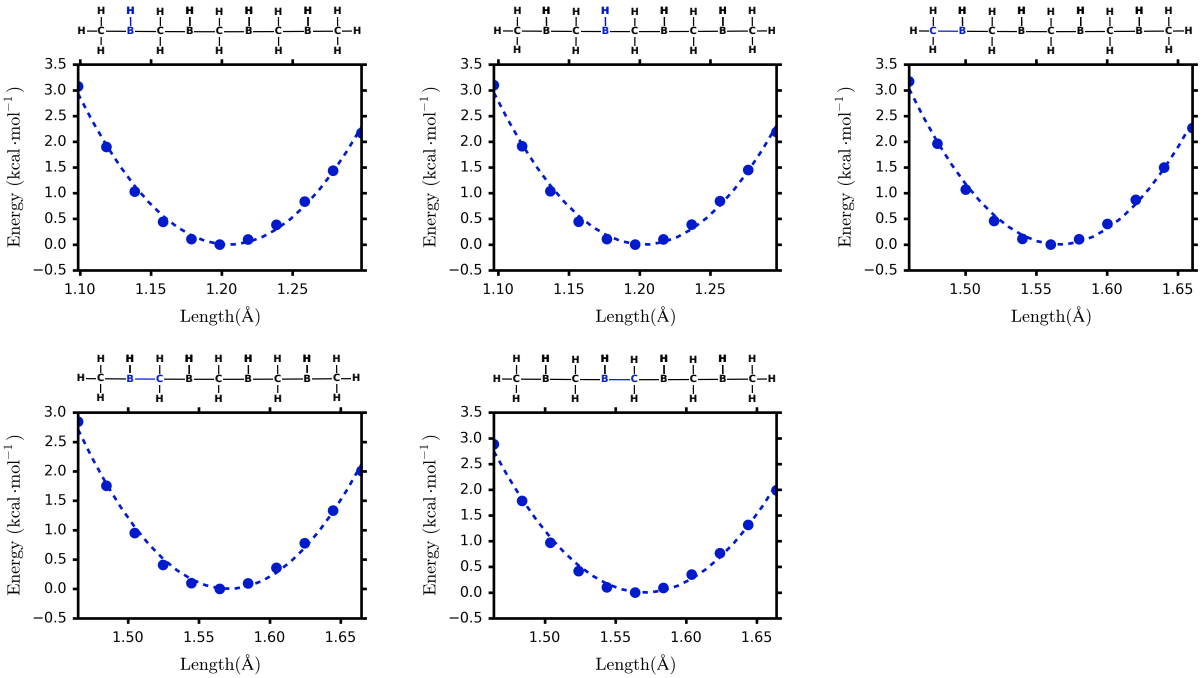

Figure S14: HBC bond potentials (blue dots) calculated at the B3LYP-D3/def2-TZVP level of theory, shown with harmonic fits (dotted lines). The energy minima have been set to zero.

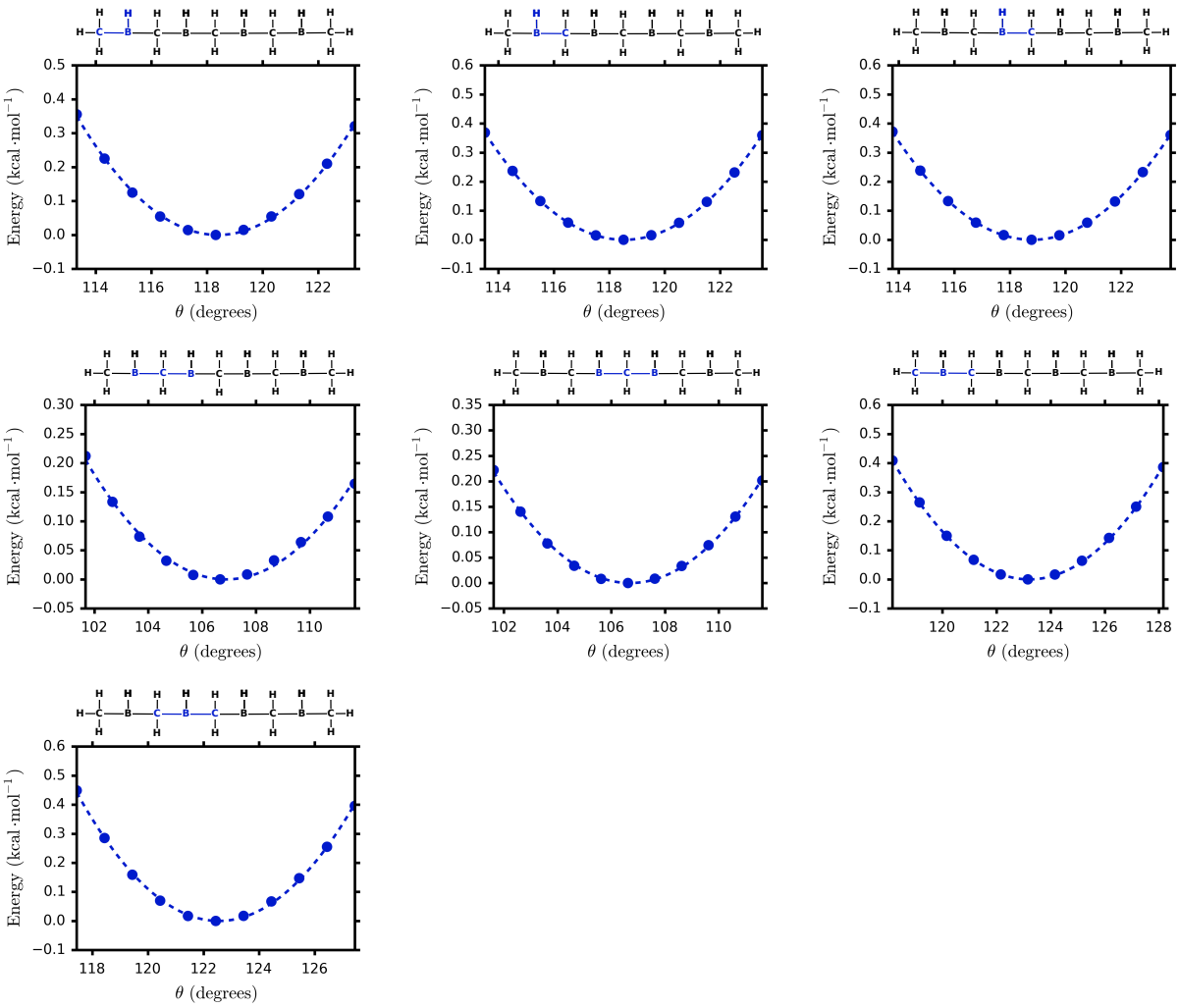

Figure S15: HBC angle potentials (blue dots) calculated at the B3LYP-D3/def2-TZVP level of theory, shown with harmonic fits (dotted lines). The energy minima have been set to zero.

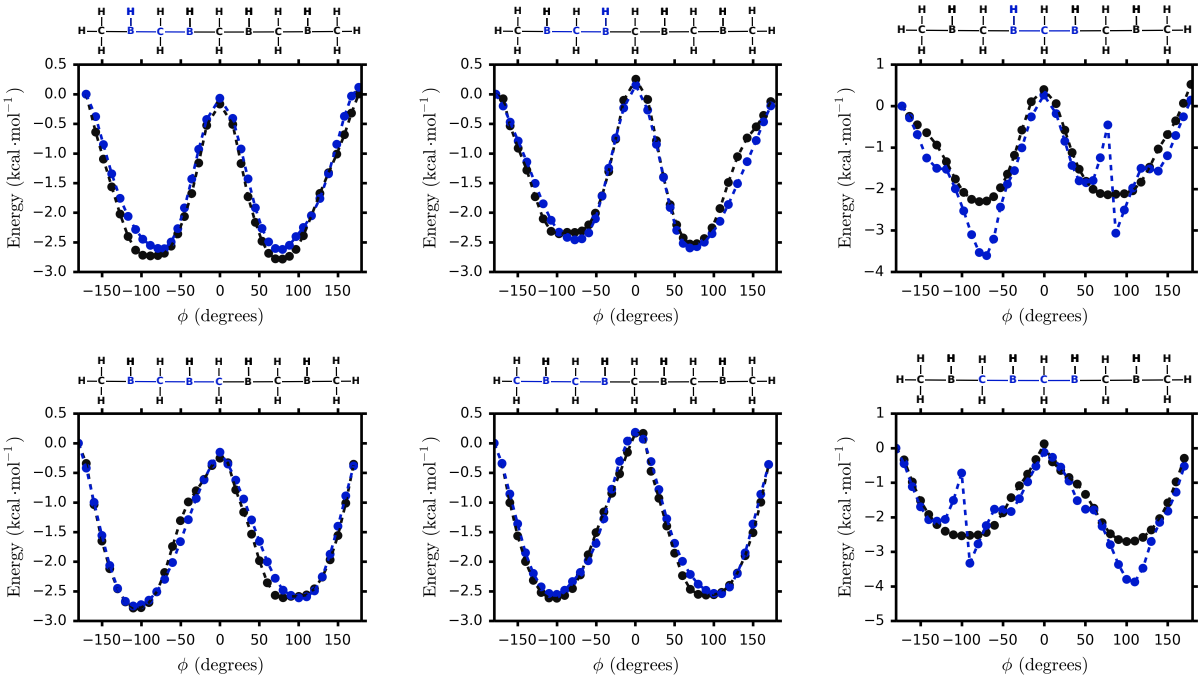

Figure S16: HBC dihedral potentials (black dots) calculated at the B3LYP-D3/def2-TZVP level of theory, shown with fits to the OPLS potential (blue dots). The configuration closest to -180° has been set to zero in each plot.

6.5 HBCC Bond, Angle, and Dihedral Fits

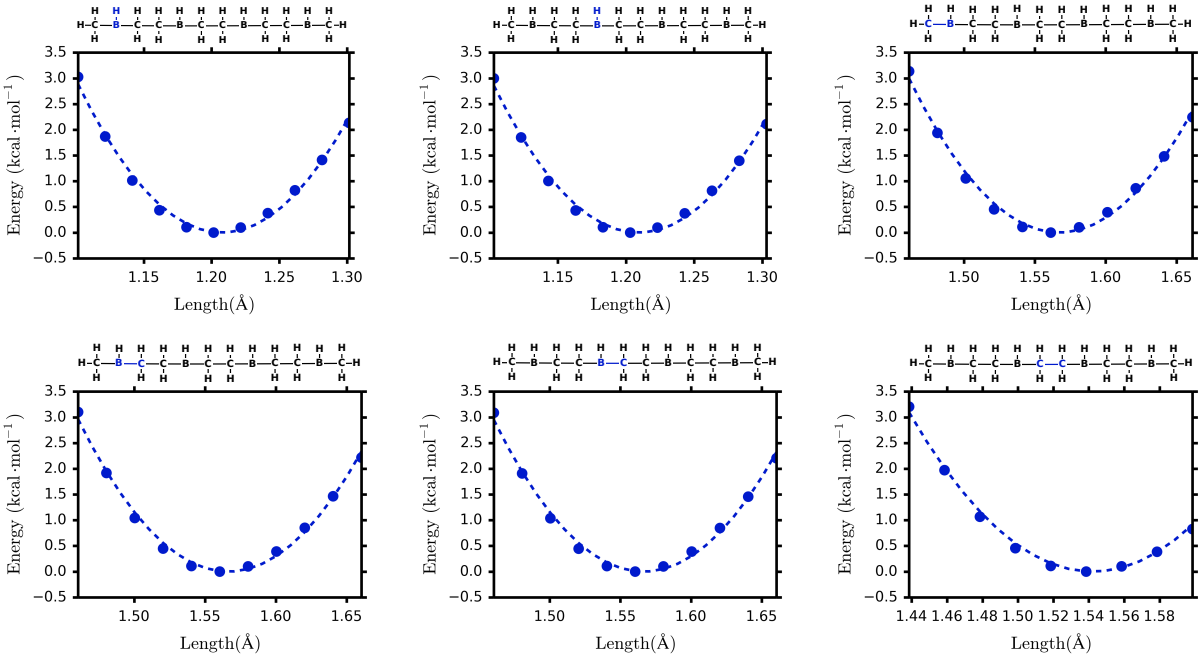

Figure S17: HBCC bond potentials (blue dots) calculated at the B3LYP-D3/def2-TZVP level of theory, shown with harmonic fits (dotted lines). The energy minima have been set to zero.

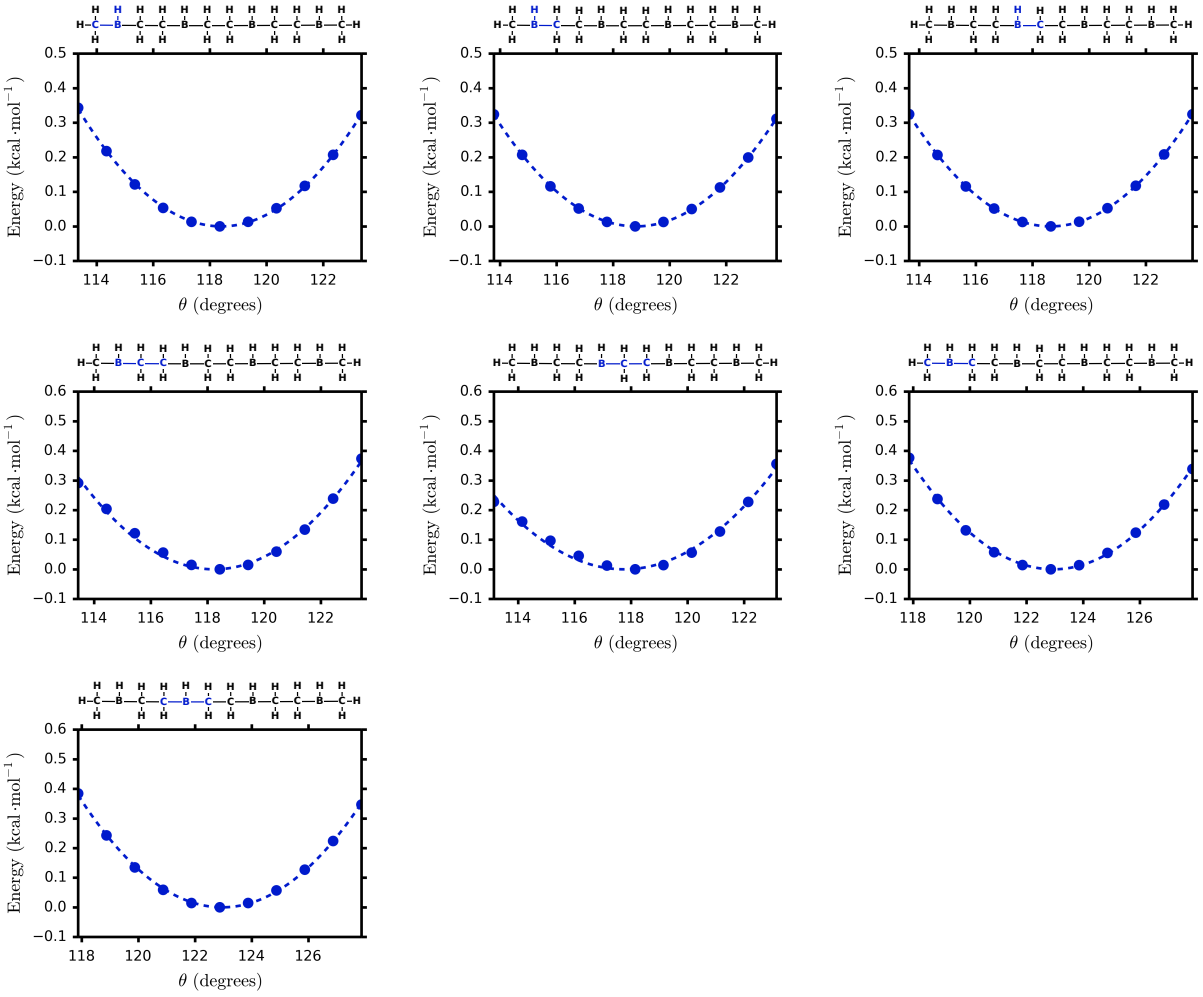

Figure S18: HBCC angle potentials (blue dots) calculated at the B3LYP-D3/def2-TZVP level of theory, shown with harmonic fits (dotted lines). The energy minima have been set to zero.

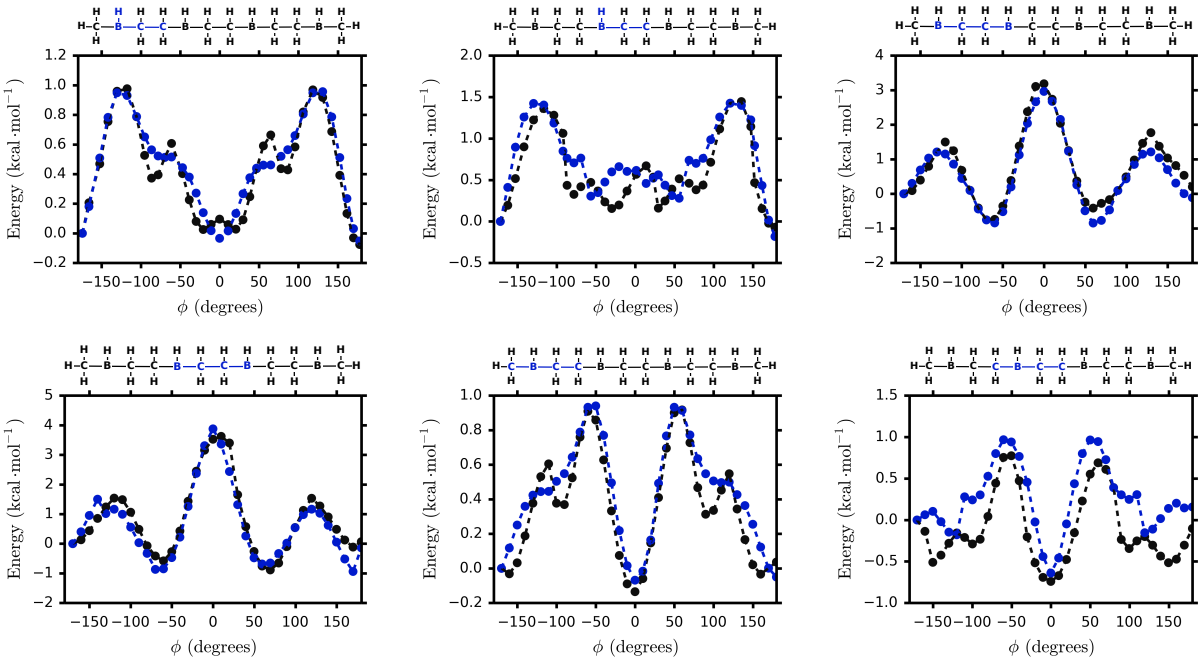

Figure S19: HBCC dihedral potentials (black dots) calculated at the B3LYP-D3/def2-TZVP level of theory, shown with fits to the OPLS potential (blue dots). The configuration closest to -180° has been set to zero in each plot.

6.6 Triflate Bond, Angle, and Dihedral Fits

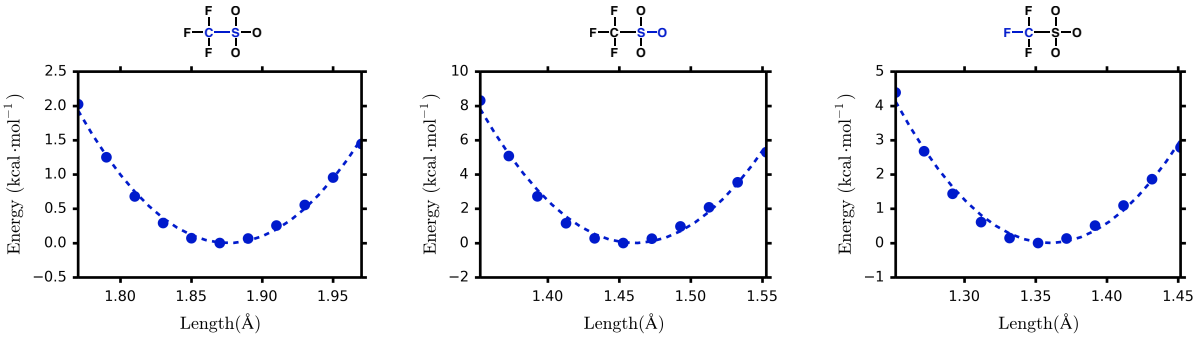

Figure S20: Triflate bond potentials (blue dots) calculated at the B3LYP-D3/def2-TZVP level of theory, shown with harmonic fits (dotted lines). The energy minima have been set to zero.

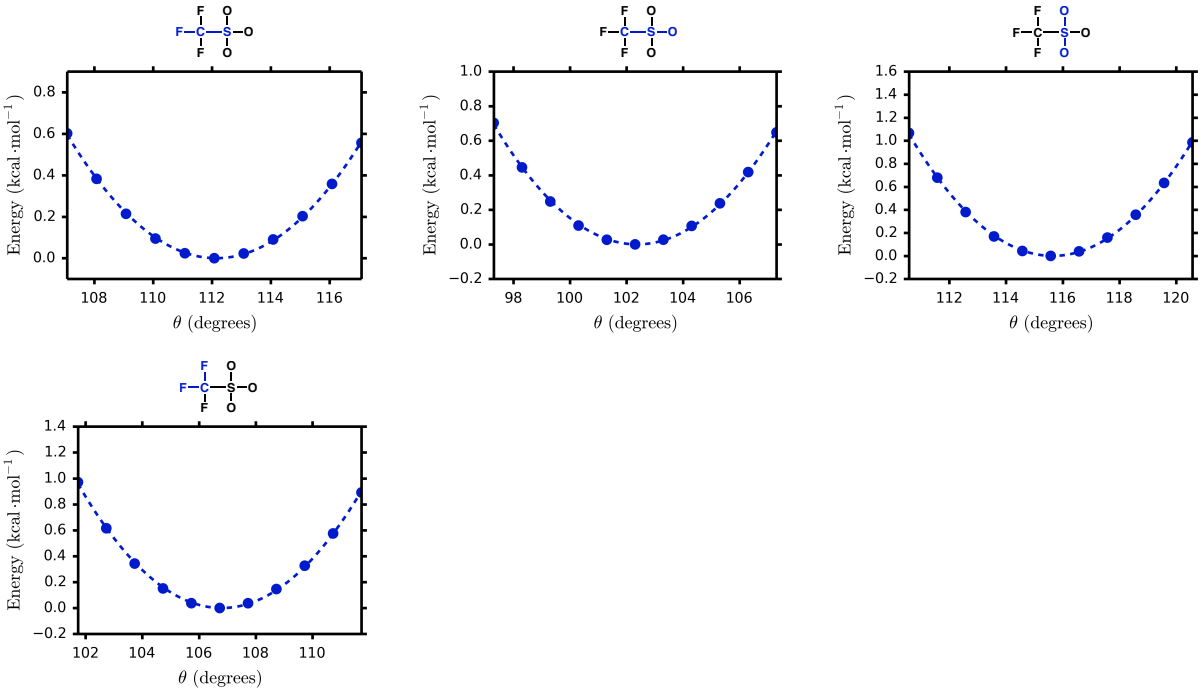

Figure S21: Triflate angle potentials (blue dots) calculated at the B3LYP-D3/def2-TZVP level of theory, shown with harmonic fits (dotted lines). The energy minima have been set to zero.

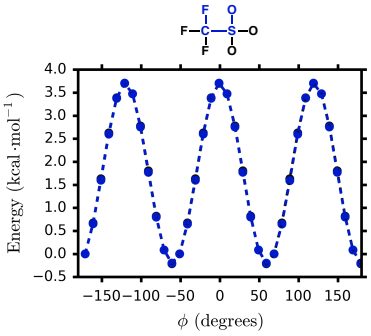

Figure S22: Triflate dihedral potentials (black dots) calculated at the B3LYP-D3/def2-TZVP level of theory, shown with fits to the OPLS potential (blue dots). The configuration closest to -180° has been set to zero in each plot.

6.7 $TFSI^-$ Bond, Angle, and Dihedral Fits

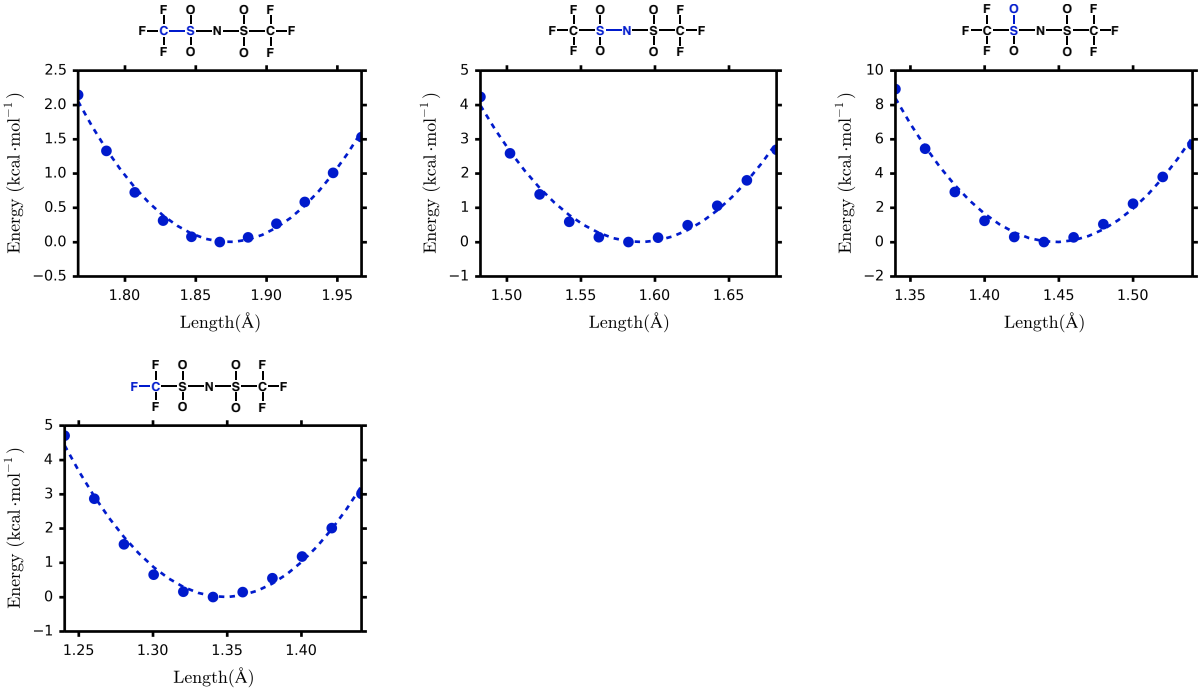

Figure S23: $TFSI^-$ bond potentials (blue dots) calculated at the B3LYP-D3/def2-TZVP level of theory, shown with harmonic fits (dotted lines). The energy minima have been set to zero.

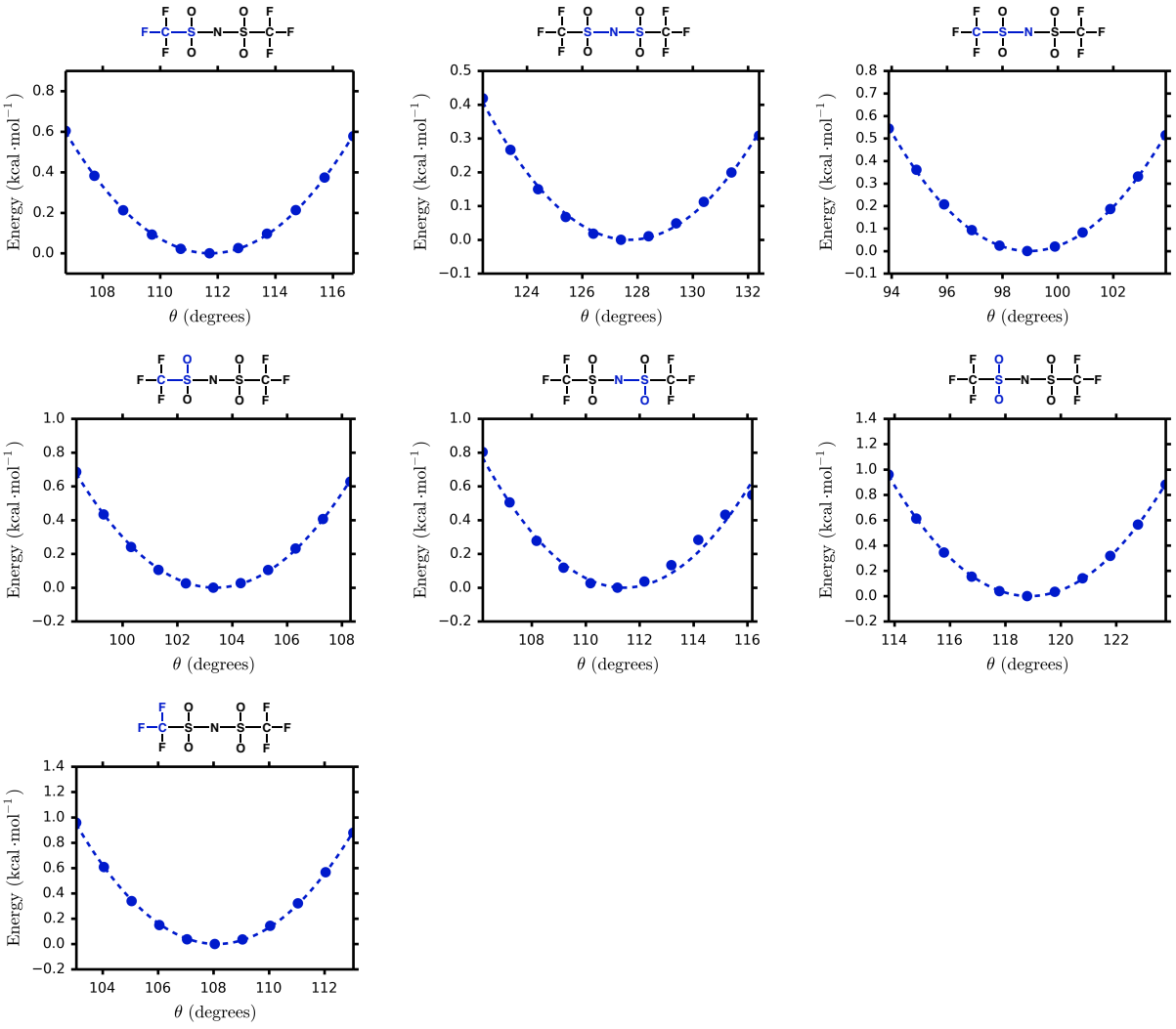

Figure S24: TFSI$^-$ angle potentials (blue dots) calculated at the B3LYP-D3/def2-TZVP level of theory, shown with harmonic fits (dotted lines). The energy minima have been set to zero.

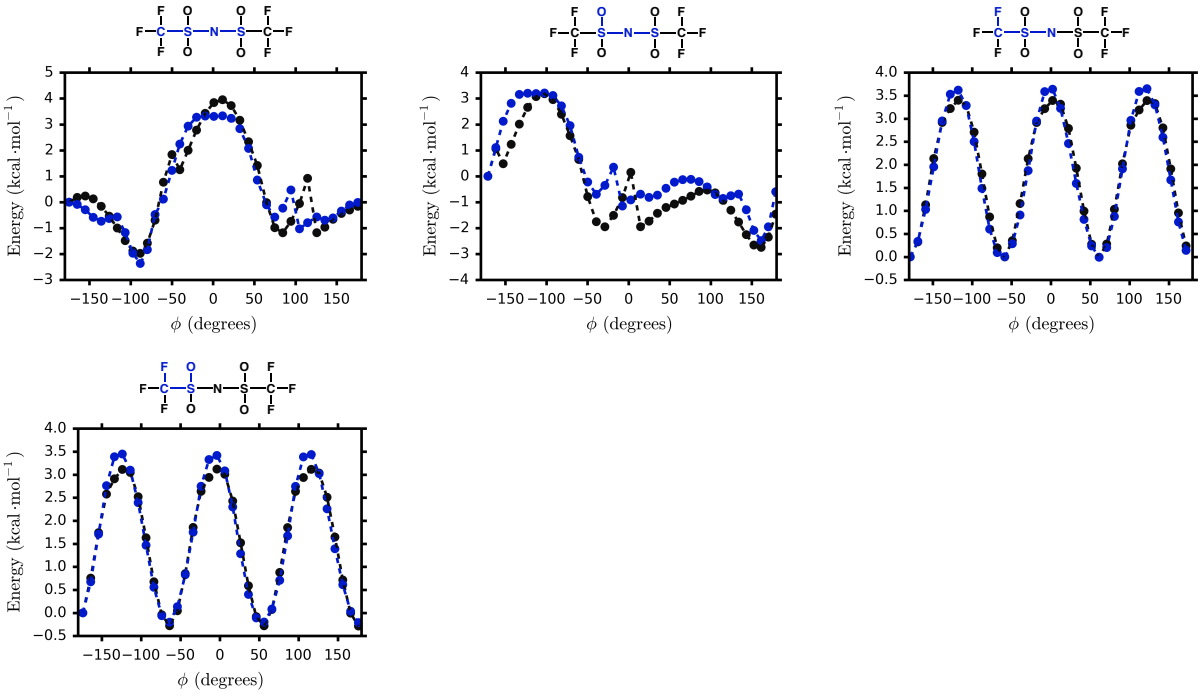

Figure S25: TFSI$^-$ dihedral potentials (black dots) calculated at the B3LYP-D3/def2-TZVP level of theory, shown with fits to the OPLS potential (blue dots). The configuration closest to -180° has been set to zero in each plot.

7 Force-Field Fit Potentials: Lennard-Jones Parameters

7.1 PEO Lennard-Jones Fits

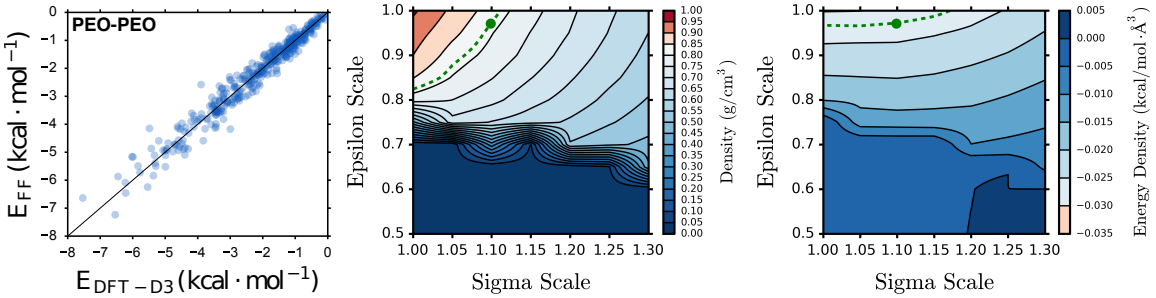

Figure S26: Fit of united-atom polymer-polymer Lennard-Jones interactions. (left) B3LYP-D3/def2-TZVP interaction energies (E_{DFT-D3}) compared with force-field interaction energies (E_{FF}) for all pair configurations included in the fit set. The B3LYP-D3/def2-TZVP interaction energy reflects the counterpoise-corrected interaction energy and the FF interaction energy reflects the sum of intermolecular electrostatic and LJ potentials at the all-atom level of representation. (middle) The dependence of the united-atom mass density on the uniform scaling of the united-atom epsilon and sigma values. (right) The dependence of the united-atom vdw energy density on the uniform scaling of the united-atom epsilon and sigma values. The contours in the middle and right plots depict the epsilon and sigma values that reproduce the all-atom mass density and energy density; the green dot represents the combination of scaling values that simultaneously reproduce both the all-atom mass density and energy density at the united-atom level of description.

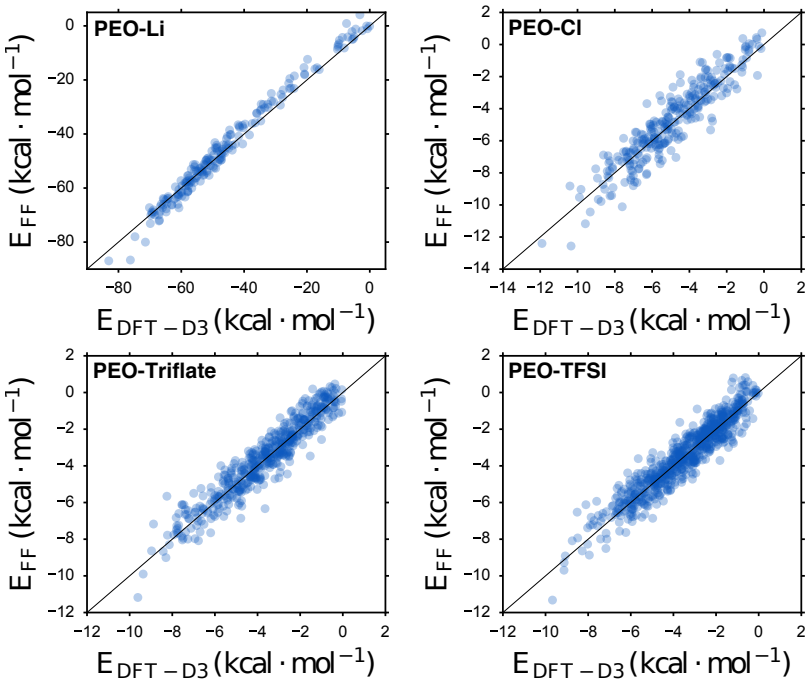

Figure S27: Fit of the united-atom polymer-ion Lennard-Jones interactions. Each plot presents the B3LYP-D3/def2-TZVP interaction energies (E_{DFT-D3}) compared with force-field interaction energies (E_{FF}) for all pair-configurations included in the fit set. The B3LYP-D3/def2-TZVP interaction energy reflects the counterpoise-corrected interaction energy and the FF interaction energy reflects the sum of intermolecular electrostatic and LJ potentials. All fits were performed with the united-atom approximation.

7.2 CBC Lennard-Jones Fits

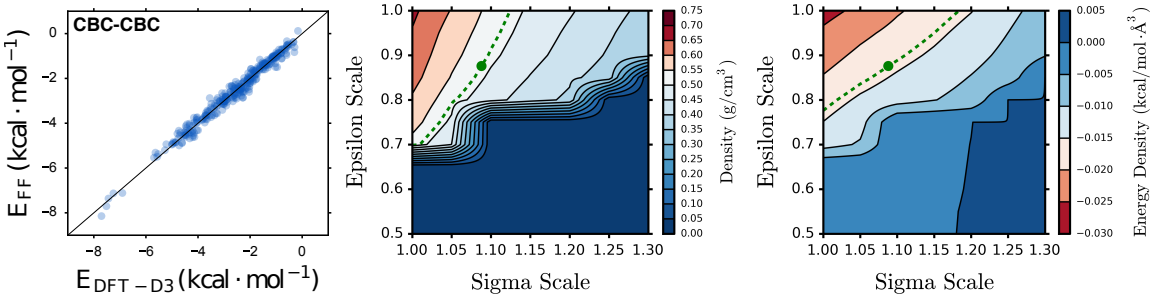

Figure S28: Fit of united-atom polymer-polymer Lennard-Jones interactions. (left) B3LYP-D3/def2-TZVP interaction energies (E_{DFT-D3}) compared with force-field interaction energies (E_{FF}) for all pair configurations included in the fit set. The B3LYP-D3/def2-TZVP interaction energy reflects the counterpoise-corrected interaction energy and the FF interaction energy reflects the sum of intermolecular electrostatic and LJ potentials at the all-atom level of representation. (middle) The dependence of the united-atom mass density on the uniform scaling of the united-atom epsilon and sigma values. (right) The dependence of the united-atom vdw energy density on the uniform scaling of the united-atom epsilon and sigma values. The contours in the middle and right plots depict the epsilon and sigma values that reproduce the all-atom mass density and energy density; the green dot represents the combination of scaling values that simultaneously reproduce both the all-atom mass density and energy density at the united-atom level of description.

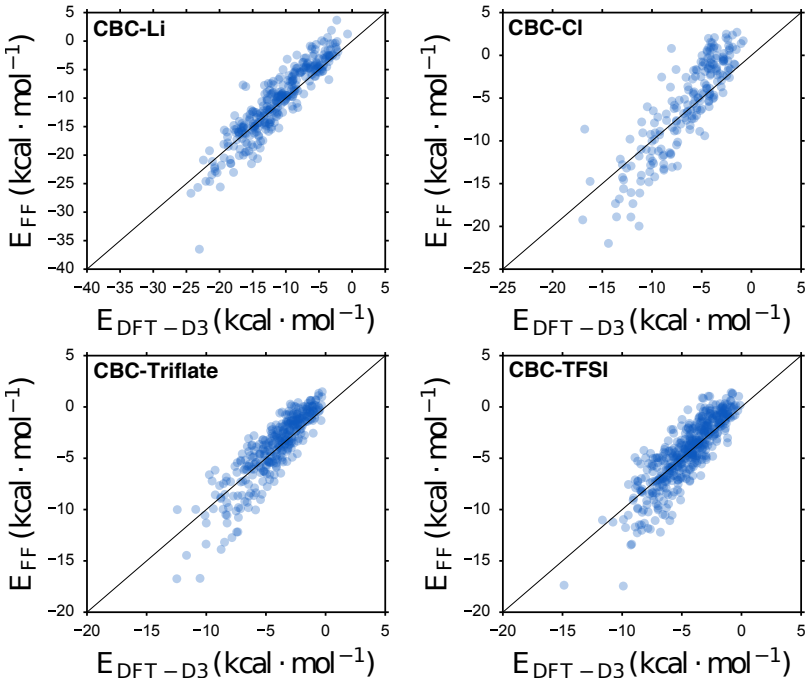

Figure S29: Fit of the united-atom polymer-ion Lennard-Jones interactions. Each plot presents the B3LYP-D3/def2-TZVP interaction energies (E_{DFT-D3}) compared with force-field interaction energies (E_{FF}) for all pair-configurations included in the fit set. The B3LYP-D3/def2-TZVP interaction energy reflects the counterpoise-corrected interaction energy and the FF interaction energy reflects the sum of intermolecular electrostatic and LJ potentials. All fits were performed with the united-atom approximation.

7.3 CBCC Lennard-Jones Fits

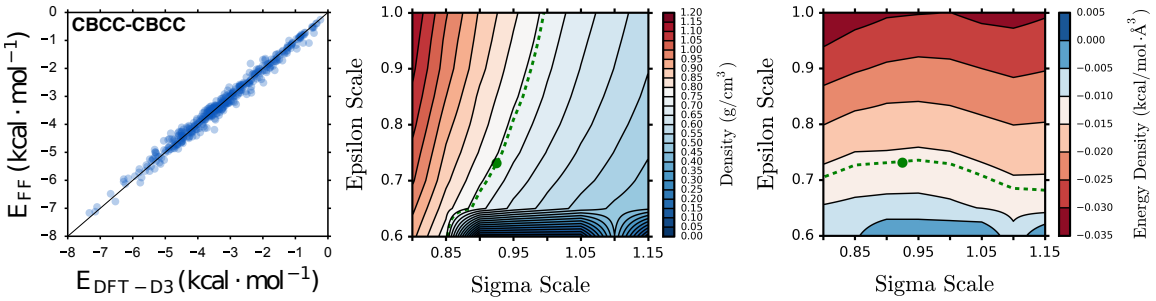

Figure S30: Fit of united-atom polymer-polymer Lennard-Jones interactions. (left) B3LYP-D3/def2-TZVP interaction energies (E_{DFT-D3}) compared with force-field interaction energies (E_{FF}) for all pair configurations included in the fit set. The B3LYP-D3/def2-TZVP interaction energy reflects the counterpoise-corrected interaction energy and the FF interaction energy reflects the sum of intermolecular electrostatic and LJ potentials at the all-atom level of representation. (middle) The dependence of the united-atom mass density on the uniform scaling of the united-atom epsilon and sigma values. (right) The dependence of the united-atom vdw energy density on the uniform scaling of the united-atom epsilon and sigma values. The contours in the middle and right plots depict the epsilon and sigma values that reproduce the all-atom mass density and energy density; the green dot represents the combination of scaling values that simultaneously reproduce both the all-atom mass density and energy density at the united-atom level of description.

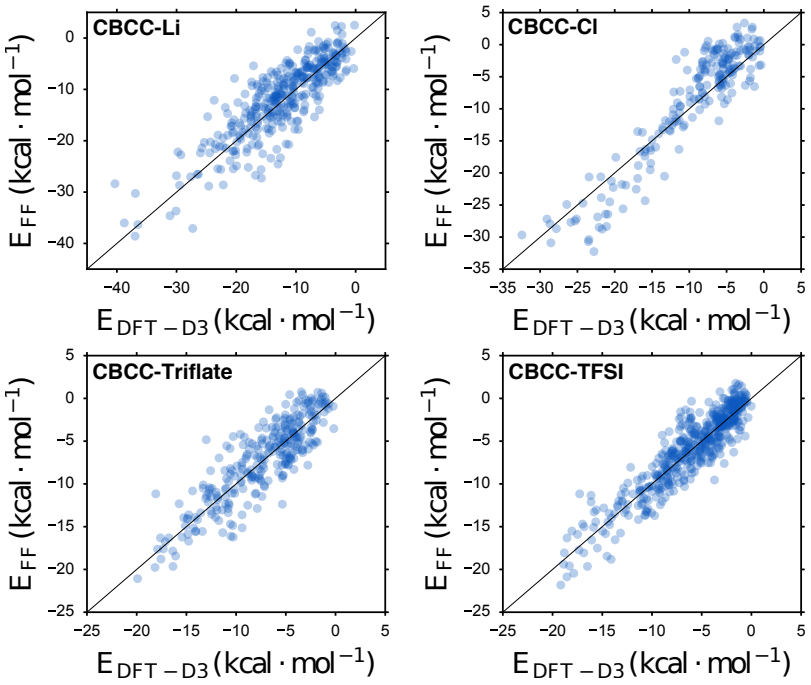

Figure S31: Fit of the united-atom polymer-ion Lennard-Jones interactions. Each plot presents the B3LYP-D3/def2-TZVP interaction energies (E_{DFT-D3}) compared with force-field interaction energies (E_{FF}) for all pair-configurations included in the fit set. The B3LYP-D3/def2-TZVP interaction energy reflects the counterpoise-corrected interaction energy and the FF interaction energy reflects the sum of intermolecular electrostatic and LJ potentials. All fits were performed with the united-atom approximation.

7.4 HBC Lennard-Jones Fits

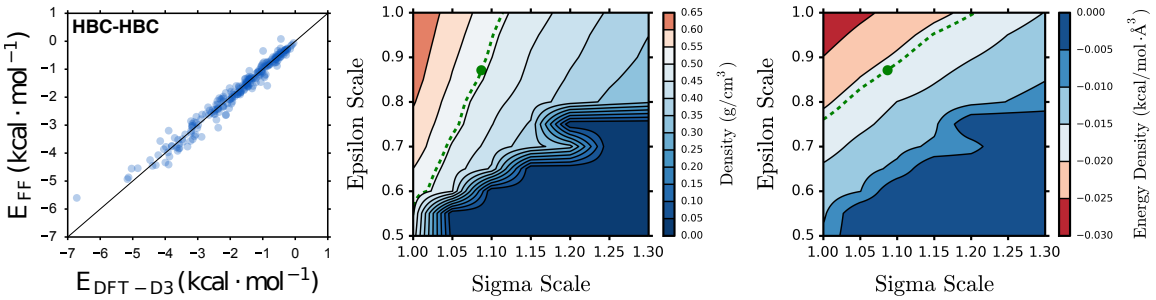

Figure S32: Fit of united-atom polymer-polymer Lennard-Jones interactions. (left) B3LYP-D3/def2-TZVP interaction energies (E_{DFT-D3}) compared with force-field interaction energies (E_{FF}) for all pair configurations included in the fit set. The B3LYP-D3/def2-TZVP interaction energy reflects the counterpoise-corrected interaction energy and the FF interaction energy reflects the sum of intermolecular electrostatic and LJ potentials at the all-atom level of representation. (middle) The dependence of the united-atom mass density on the uniform scaling of the united-atom epsilon and sigma values. (right) The dependence of the united-atom vdw energy density on the uniform scaling of the united-atom epsilon and sigma values. The contours in the middle and right plots depict the epsilon and sigma values that reproduce the all-atom mass density and energy density; the green dot represents the combination of scaling values that simultaneously reproduce both the all-atom mass density and energy density at the united-atom level of description.

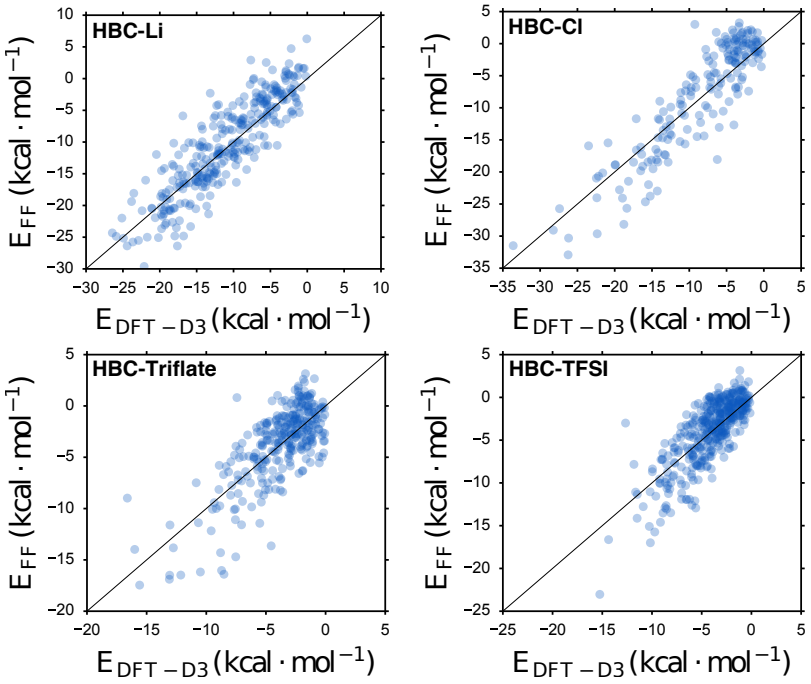

Figure S33: Fit of the united-atom polymer-ion Lennard-Jones interactions. Each plot presents the B3LYP-D3/def2-TZVP interaction energies (E_{DFT-D3}) compared with force-field interaction energies (E_{FF}) for all pair-configurations included in the fit set. The B3LYP-D3/def2-TZVP interaction energy reflects the counterpoise-corrected interaction energy and the FF interaction energy reflects the sum of intermolecular electrostatic and LJ potentials. All fits were performed with the united-atom approximation.

7.5 HBCC Lennard-Jones Fits

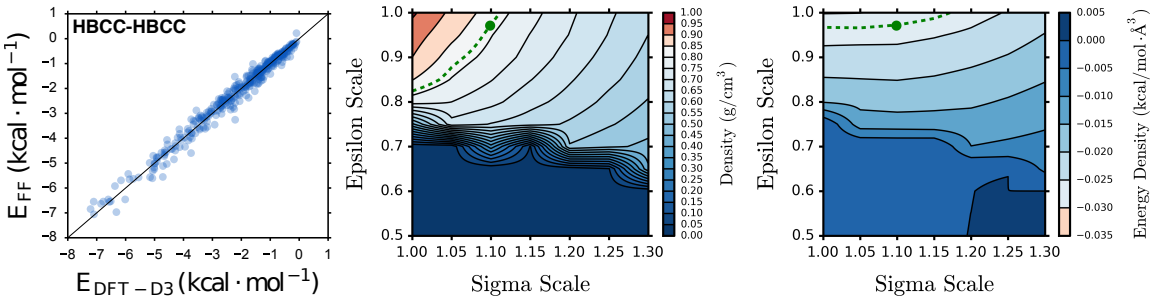

Figure S34: Fit of united-atom polymer-polymer Lennard-Jones interactions. (left) B3LYP-D3/def2-TZVP interaction energies (E_{DFT-D3}) compared with force-field interaction energies (E_{FF}) for all pair configurations included in the fit set. The B3LYP-D3/def2-TZVP interaction energy reflects the counterpoise-corrected interaction energy and the FF interaction energy reflects the sum of intermolecular electrostatic and LJ potentials at the all-atom level of representation. (middle) The dependence of the united-atom mass density on the uniform scaling of the united-atom epsilon and sigma values. (right) The dependence of the united-atom vdw energy density on the uniform scaling of the united-atom epsilon and sigma values. The contours in the middle and right plots depict the epsilon and sigma values that reproduce the all-atom mass density and energy density; the green dot represents the combination of scaling values that simultaneously reproduce both the all-atom mass density and energy density at the united-atom level of description.

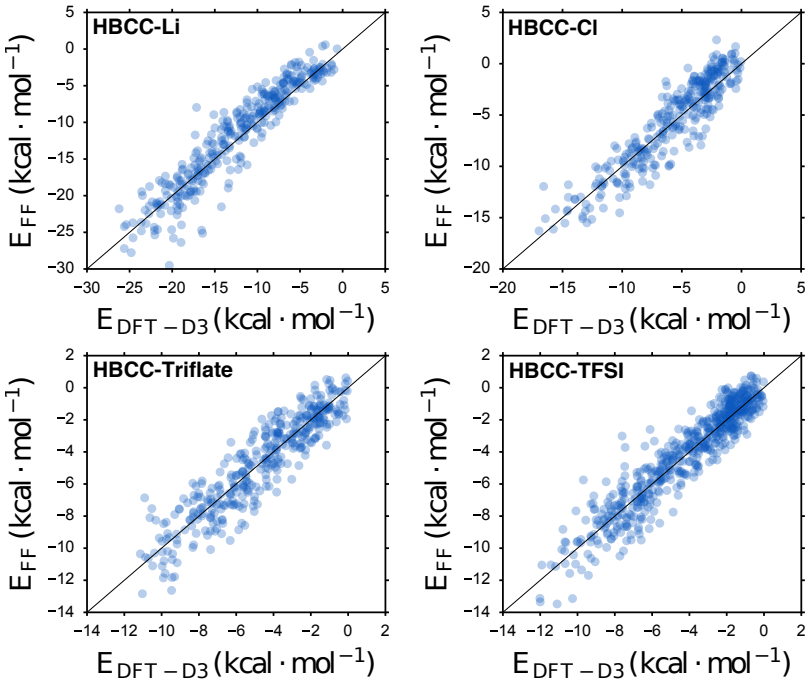

Figure S35: Fit of the united-atom polymer-ion Lennard-Jones interactions. Each plot presents the B3LYP-D3/def2-TZVP interaction energies (E_{DFT-D3}) compared with force-field interaction energies (E_{FF}) for all pair-configurations included in the fit set. The B3LYP-D3/def2-TZVP interaction energy reflects the counterpoise-corrected interaction energy and the FF interaction energy reflects the sum of intermolecular electrostatic and LJ potentials. All fits were performed with the united-atom approximation.

7.6 Li-Anion Lennard-Jones Fits

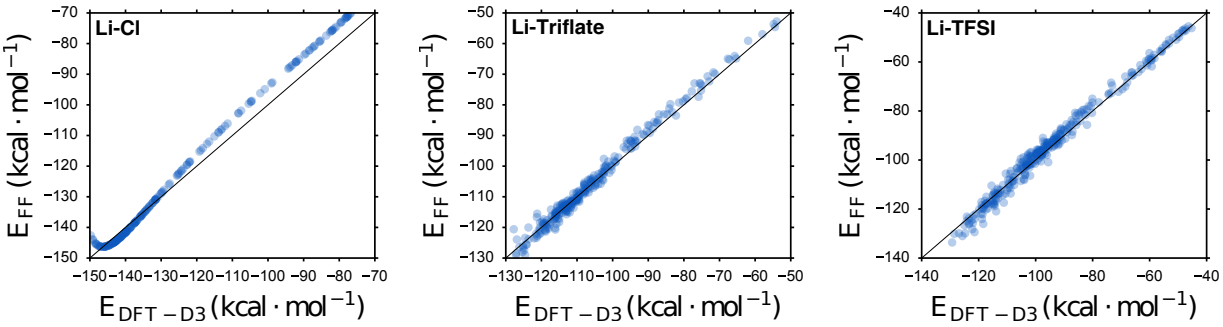

Figure S36: Fits of the Li-anion Lennard-Jones interactions. Each plot presents the B3LYP-D3/def2-TZVP interaction energies (E_{DFT-D3}) compared with force-field interaction energies (E_{FF}) for all pair-configurations included in the fit set. The B3LYP-D3/def2-TZVP interaction energy reflects the counterpoise-corrected interaction energy and the FF interaction energy reflects the sum of intermolecular electrostatic and LJ potentials. The inadequate treatment of polarizability is clearly represented in the LiCl fit, where the optimum parameters reflect a trade-off in accurately representing the potential minimum and long-range decay of the binding potential.

References

1. Plimpton, S. Fast parallel algorithms for short-range molecular dynamics. *J. Comput. Phys.* **117**, 1–19 (1994).

2. Borodin, O. & Smith, G. D. Mechanism of ion transport in amorphous poly(ethylene oxide)/LiTFSI from molecular dynamics simulations. *Macromolecules* **39**, 1620–1629 (2006).

3. Webb, M. A. *et al.* Systematic computational and experimental investigation of lithium-ion transport mechanisms in polyester-based polymer electrolytes. *ACS Cent. Sci.* (2015).

4. Frenkel, D. & Smit, B. *Understanding Molecular Simulation: From Algorithms to Applications* (Academic Press, 2001), 2nd edn.

5. Beutler, T. C., Mark, A. E., van Schaik, R. C., Gerber, P. R. & van Gunsteren, W. F. Avoiding singularities and numerical instabilities in free energy calculations based on molecular simulations. *Chem. Phys. Lett.* **222**, 529–539 (1994).

6. Efron, B. & Tibshirani, R. J. *An Introduction to the Bootstrap* (Chapman and Hall/CRC, 1993), 1st edn.

7. Onak, T. *Organoborane Chemistry.* Organometallic Chemistry Series (Academic Press, 1975).

8. Jenkins, H., Roobottom, H., Passmore, J. & Glasser, L. Relationships among ionic lattice energies, molecular (formula unit) volumes, and thermochemical radii. *Inorg. Chem.* **38**, 3609–3620 (1998). URL `http://pubs.acs.org/doi/abs/10.1021/ic9812961`.

9. Müller-Plathe, F. Permeation of polymers - a computational approach. *Acta Polymer* **45**, 259–293 (1994).

10. Müller-Plathe, F. & Van Gunsteren, W. Computer simulation of a polymer electrolyte: Lithium iodide in amorphous poly(ethylene oxide). *J. Chem. Phys.* **103**, 4745 (1994).

11. Lin, K. & Maranas, J. Superionic behavior in polyethylene-oxide–based single-ion conductors. *Phys. Rev. E* **88**, 052602 (2013).

12. Lin, K. & Maranas, J. Does decreasing ion–ion association improve cation mobility in single ion conductors? *Phys. Chem. Chem. Phys.* **15**, 16143 (2013).

13. Chaudhari, M. *et al.* Scaling atomic partial charges of carbonate solvents for lithium ion solvation and diffusion. *J. Chem. Theory Comput.* **12**, 5709–5718 (2016). URL `http://pubs.acs.org/doi/abs/10.1021/acs.jctc.6b00824`.

14. Grimme, S., Antony, J., Ehrlich, S. & Krieg, H. A consistent and accurate ab initio parametrization of density functional dispersion correction (dft-d) for the 94 elements h-pu. *J. Chem. Phys.* **132**, 154104 (2010). URL `http://scitation.aip.org/content/aip/journal/jcp/132/15/10.1063/1.3382344`.

15. Weigend, F. & Ahlrichs, R. Balanced basis sets of split valence, triple zeta valence and quadruple zeta valence quality for h to rn: design and assessment of accuracy. *Physical Chemistry Chemical Physics* **7**, 3297–3305 (2005). URL `http://pubs.rsc.org/en/content/articlehtml/2005/cp/b508541a`.

16. Zheng, J., Xu, X. & Truhlar, D. Minimally augmented karlsruhe basis sets. *Theor. Chem. Acc.* **128**, 295–305 (2011). URL http://link.springer.com/article/10.1007/s00214-010-0846-z.

17. Breneman, C. M. & Wiberg, K. B. Determining atom-centered monopoles from molecular electrostatic potentials. the need for high sampling density in formamide conformational analysis. *J. Comp. Chem.* **11**, 361–373 (1990). URL http://dx.doi.org/10.1002/jcc.540110311.

18. Jorgensen, W., Maxwell, D. & Tirado-Rives, J. Development and testing of the opls all-atom force field on conformational energetics and properties of organic liquids. *J. Am. Chem. Soc.* **118**, 11225–11236 (1995). URL http://pubs.acs.org/doi/abs/10.1021/ja9621760.

19. Rappe, A. K., Casewit, C. J., Colwell, K. S., Goddard, W. A. & Skiff, W. M. Uff, a full periodic table force field for molecular mechanics and molecular dynamics simulations. *J. Am. Chem. Soc.* **114**, 10024–10035 (1992).

20. Wick, C. D. & Theodorou, D. N. Connectivity-altering monte carlo simulations of the end group effects on volumetric properties for poly(ethylene oxide). *Macromolecules* **37**, 7026–7033 (2004). URL http://dx.doi.org/10.1021/ma049193r.

21. Borodin, O., Douglas, R., Smith, G. D., Trouw, F. & Petrucci, S. Md simulations and experimental study of structure, dynamics, and thermodynamics of poly(ethylene oxide) and its oligomers. *J. Phys. Chem. B* **107**, 6813–6823 (2003). URL http://dx.doi.org/10.1021/jp0275387.

22. Hyun, J.-K., Dong, H., Rhodes, C. P., Frech, R. & Wheeler, R. A. Molecular dynamics simulations and spectroscopic studies of amorphous tetraglyme (ch3o(ch2ch2o)4ch3) and tetraglyme:licf3so3 structures. *J. Phys. Chem. B* **105**, 3329–3337 (2001). URL http://dx.doi.org/10.1021/jp003591o.

23. Edman, L., Ferry, A. & Orädd, G. Analysis of diffusion in a solid polymer electrolyte in the context of a phase-separated system. *Phys. Rev. E* **65**, 042803 (2002).

24. Lightfoot, P., Nowinski, J. & Bruce, P. crystal structures of the polymer electrolytes poly (ethylene oxide) 4: Mscn (m= nh4, k). *J. Am. Chem. Soc.* **116**, 7469–7470 (1994). URL http://pubs.acs.org/doi/abs/10.1021/ja00095a085.

25. Henderson, W., Brooks, N. & Young, V. Single-crystal structures of polymer electrolytes. *J. Am. Chem. Soc.* **125**, 12098–12099 (2003). URL http://pubs.acs.org/doi/abs/10.1021/ja036535k.

26. Andreev, Y. *et al.* Crystal structures of poly (ethylene oxide) 3: Libf4 and (diglyme) n: Libf4 (n= 1, 2). *Chem. Mater.* **17** (2005). URL http://pubs.acs.org/doi/abs/10.1021/cm048310u.

27. Halley, J. W., Duan, Y., Curtiss, L. A. & Baboul, A. G. Lithium perchlorate ion pairing in a model of amorphous polyethylene oxide. *J. Chem. Phys.* **111**, 3302–3308 (1999). URL http://scitation.aip.org/content/aip/journal/jcp/111/7/10.1063/1.479609.

28. Webb, M. A., Savoie, B. M., Wang, Z.-G. & Miller III, T. F. Chemically specific dynamic bond percolation model for ion transport in polymer electrolytes. *Macromolecules* **48**, 7346–7358 (2015). URL http://dx.doi.org/10.1021/acs.macromol.5b01437.

29. Borodin, O. & Smith, G. D. Development of many-body polarizable force fields for Li-battery applications: 2. LiTFSI-doped oligoether, polyether, and carbonate-based electrolytes. *J. Phys. Chem. B* **110**, 6293–6299 (2006).

30. Borodin, O. Polarizable force field development and molecular dynamics simulations of ionic liquids. *J. Phys. Chem. B* **113**, 11463–11478 (2009).